APL Materials

RESEARCH ARTICLE | OCTOBER 22 2025

Growth of conductive Si-doped α-Ga_2O_3 by suboxide molecular-beam epitaxy

Jacob Steele ; Julianne Chen ; Tamá Burrell; Naomi A. Pieczulewski ; Debaditya Bhattacharya ; Kathleen Smith ; Katie Gann ; Michael O. Thompson ; Huili G. Xing ; Debdeep Jena ; David A. Muller ; Michael D. Williams ; M. K. Indika Senevirathna ; Darrell G. Schlom

APL Mater. 13, 101117 (2025)
https://doi.org/10.1063/5.0299750

AIP Publishing

Growth of conductive Si-doped α-Ga_2O_3 by suboxide molecular-beam epitaxy

Cite as: APL Mater. 13, 101117 (2025); doi: 10.1063/5.0299750
Submitted: 28 August 2025 • Accepted: 30 September 2025 •
Published Online: 22 October 2025

View Online Export Citation CrossMark

Jacob Steele,[1] Julianne Chen,[2] Tamá Burrell,[3] Naomi A. Pieczulewski,[1] Debaditya Bhattacharya,[4] Kathleen Smith,[4] Katie Gann,[1] Michael O. Thompson,[1] Huili G. Xing,[1,4,5] Debdeep Jena,[1,4,5] David A. Muller,[5,6] Michael D. Williams,[3] M. K. Indika Senevirathna,[3] and Darrell G. Schlom[1,5,7,a)]

AFFILIATIONS

[1] Department of Materials Science and Engineering, Cornell University, Ithaca, New York 14853, USA
[2] Platform for the Accelerated Realization, Analysis, and Discovery of Interface Materials (PARADIM), Cornell University, Ithaca, New York 14853, USA
[3] Department of Physics, Clark Atlanta University, Atlanta, Georgia 30314, USA
[4] School of Electrical and Computer Engineering, Cornell University, Ithaca, New York 14853, USA
[5] Kavli Institute at Cornell for Nanoscale Science, Ithaca, New York 14853, USA
[6] School of Applied and Engineering Physics, Cornell University, Ithaca, New York 14853, USA
[7] Leibniz-Institut für Kristallzüchtung, Max-Born-Str. 2, 12489 Berlin, Germany

[a)] **Author to whom correspondence should be addressed:** schlom@cornell.edu

ABSTRACT

We report a two-step film-growth process using suboxide molecular-beam epitaxy (*S*-MBE) that produces Si-doped α-Ga_2O_3 with record transport properties. The method involves growing a relaxed α-$(Al_xGa_{1-x})_2O_3$ buffer layer on *m*-plane sapphire at a relatively high substrate temperature (T_{sub}), ~750 °C, followed by an Si-doped α-Ga_2O_3 overlayer grown at lower T_{sub}, ~500 °C. The high T_{sub} allows the ~3.6% lattice-mismatched α-$(Al_xGa_{1-x})_2O_3$ buffer with $x = 0.08 \pm 0.02$ to remain epitaxial and phase pure during relaxation to form a pseudosubstrate for the overgrowth of α-Ga_2O_3. The optimal conditions for the subsequent growth of Si-doped α-Ga_2O_3 by *S*-MBE are 425 °C ≤ T_{sub} ≤ 500 °C and $P_{80\%\ O3} = 5 \times 10^{-6}$ Torr. Si-doped α-Ga_2O_3 films grown with this method at $T_{sub} > 550$ °C are always insulating. Secondary-ion mass spectrometry confirms that both the insulating and conductive films have uniform silicon incorporation. In conductive films with $10^{19} \le N_{Si} \le 10^{20}$ cm^{-3}, the incorporated silicon is ~100% electrically active. At $N_{Si} \le 10^{19}$ cm^{-3}, the carrier concentration (n) plummets. A maximum Hall mobility (μ) = 90 $\frac{cm^2}{V \cdot s}$ at room-temperature is measured in a film with $n = 2.9 \times 10^{19}$ cm^{-3} and a maximum conductivity (σ) = 650 S/cm at room-temperature in a film with $n = 4.8 \times 10^{19}$ cm^{-3}. A threading dislocation density of $(5.6 \pm 0.6) \times 10^{10}$ cm^{-2} is revealed by scanning transmission electron microscopy, showing that there is still enormous room to improve the electrical properties of doped α-Ga_2O_3 thin films.

INTRODUCTION

One of the most important metrics for wide and ultrawide bandgap semiconductors is the Baliga figure of merit (BFOM), which describes the theoretical minimum on-resistance for a given breakdown field of an ideal power rectifier made of a specific material.[1] The BFOM is derived to be equal to $E_c^3 \mu \varepsilon_s$, where E_c is the maximum electric field that can be applied to a semiconductor before breakdown, μ is the mobility, and ε_s is the permittivity of the semiconductor.[1] Wider bandgaps greatly increase the BFOM because E_c scales with $E_g^{\sim 1.83}$, where E_g is the bandgap of the semiconductor, resulting in the BFOM scaling with $E_g^{\sim 5.5}$ and being dominated by ultrawide bandgap materials, such as Ga_2O_3, AlN, and diamond.[2–4] Importantly, to be considered an ultrawide bandgap

semiconductor rather than an insulator, it is necessary to be able to introduce mobile carriers via doping to modulate the conductivity. Of the primary UWBG semiconductors, Ga_2O_3 has the narrowest bandgap of 4.6–5.4 eV, depending on the Ga_2O_3 polymorph. Until now, β-Ga_2O_3 has received significant attention since it has controllable *n*-type doping, room temperature electron mobilities as high as 200 $\frac{cm^2}{V \cdot s}$, and a projected critical field of 8 MV/cm and is the only ultrawide bandgap semiconductor with large-diameter (>4 in) native substrates.[4,5]

In addition to the thermodynamically stable monoclinic β phase, there are four additional phases in the Ga_2O_3 system: trigonal (α), cubic (γ and δ), and orthorhombic (κ).[1–3] Of these, the metastable α-Ga_2O_3 phase has the widest bandgap of 5.4 eV.[6] The ultrawide bandgap of α-Ga_2O_3 can be further extended to 8.6 eV by alloying with α-Al_2O_3, also increasing the breakdown field to an anticipated 30 MV/cm.[2,7] Both the bandgap and breakdown field exceed those of all known semiconductors. In addition, α-Ga_2O_3 has an electron effective mass of only $m_e^* = 0.276\ m_e^0$, where m_e^0 is the mass of a free electron and m_e^* is the effective mass of an electron in α-Ga_2O_3. This is significantly lower than the $m_e^* = 0.342\ m_e^0$ of β-Ga_2O_3.[8] The other compositional extreme, α-Al_2O_3, has an even lower reported electron effective mass of $m_e^* = 0.23\ m_e^0$, leading to a relatively high predicted electron mobility.[9]

It is predicted that the room-temperature mobility of α-Ga_2O_3 is limited by polar-optical phonons for $n \geq 10^{15}$ cm^{-3}, just as it is for β-Ga_2O_3.[6] The maximum mobility value at room temperature for α-Ga_2O_3 is predicted to be ~220 $\frac{cm^2}{V \cdot s}$, around 10% higher than the 200 $\frac{cm^2}{V \cdot s}$ maximum predicted and observed for β-Ga_2O_3.[6,10,11] Achieving the maximum mobility for α-Ga_2O_3 is expected to primarily be a challenge of finding optimal growth (including an appropriate substrate or pseudosubstrate) and doping conditions to maximize crystallinity.[6,12] For α-Al_2O_3, the theoretical room-temperature mobility is as high as 600 $\frac{cm^2}{V \cdot s}$ and the theoretical low-temperature mobility is as high as 30 000 $\frac{cm^2}{V \cdot s}$.[8,13] Given the record bandgaps and breakdown fields, as well as the high predicted mobilities, the α-$(Al_xGa_{1-x})_2O_3$ system has the potential to achieve the highest BFOM of any known semiconducting material.

Many methods have been utilized for the growth of α-$(Al_xGa_{1-x})_2O_3$ epitaxial films, including hydride vapor-phase epitaxy (HVPE),[14–16] mist chemical vapor deposition (mist CVD),[17–20] molecular-beam epitaxy (MBE),[7,21,22] metalorganic chemical vapor deposition (MOCVD),[23,24] and pulsed-laser deposition (PLD).[25,26] Using suboxide MBE (*S*-MBE) on *a*-plane sapphire, we previously demonstrated the growth of α-$(Al_xGa_{1-x})_2O_3$ with $0 < x < 0.95$ at growth rates as high as 2.9 μm/h and with the narrowest average symmetric rocking curve full width at half maximum (FWHM) of any study, 12 arc sec.[22] On *c*-plane sapphire, the highest quality α-Ga_2O_3 has been demonstrated by mist CVD and shows symmetric rocking curves with FWHM as fine as 25 arc sec.[17] On *m*-plane sapphire, HVPE has demonstrated the highest quality α-Ga_2O_3, with symmetric rocking curve FHWM as low as 1000 arc sec at growth rates of up to 6 μm/h.[16] MBE has not demonstrated phase-pure, thick α-Ga_2O_3 films on *c*-plane sapphire and has demonstrated a relatively large symmetric rocking curve FWHM of 1600 arc sec on *m*-plane sapphire.[7,27] For MBE, the *a*-plane and *c*-plane both have limited critical thicknesses for phase-pure α-Ga_2O_3 before a transition to β-Ga_2O_3 occurs.[7,28] On *m*-plane sapphire, conventional MBE has demonstrated growth across the full range of *x* with no critical thickness for phase-pure α-Ga_2O_3.[7,29] More recently, applying metal-oxide catalyzed epitaxy (MOCATAXY) to MBE growth of α-Ga_2O_3 on *m*-plane sapphire extended the growth rate up from 0.12 to 0.2 μm/h while also reducing the FWHM of the 300 α-Ga_2O_3 rocking curves from 1800 to 1600 arc sec.[27] For reasons that are not yet understood, it has also been seen in mist CVD that the mobilities of Sn-doped α-Ga_2O_3 grown on *m*-plane sapphire are significantly higher than films grown in similar conditions on *c*-plane sapphire despite worse crystallinity and similar levels of impurities.[30]

For the doping of α-Ga_2O_3, there are a wide variety of shallow *n*-type donors predicted by density functional theory (DFT), including silicon, hafnium, zirconium, tin, tantalum, and germanium.[31] With tin and silicon alone, many methods including mist CVD, PLD, MBE, MOCVD, and HVPE have successfully demonstrated conductivity in doped α-Ga_2O_3.[15,17,24,26,28,30] The highest reported α-Ga_2O_3 conductivity is 37 S/cm in an Sn-doped film with a mobile electron concentration of 1.4×10^{19} cm^{-3} grown using PLD, and the record for mobility is 65 $\frac{cm^2}{V \cdot s}$ in an Sn-doped film with a mobile electron concentration of 1.2×10^{18} cm^{-3} grown by mist CVD.[23,27] Doping with silicon has achieved a maximum mobility of 51.6 $\frac{cm^2}{V \cdot s}$ at a mobile electron concentration of 1.7×10^{18} cm^{-3} in α-Ga_2O_3 grown using HVPE.[15] We view silicon as the most promising dopant since it is expected to remain a shallow donor up to 72% aluminum incorporation, the highest of any known dopant.[31]

The limited mobilities and conductivities in doped α-Ga_2O_3 thin films are believed to be primarily due to traps from high dislocation and impurity densities. The typical substrate for growing α-Ga_2O_3 is corundum α-Al_2O_3 as it is high quality and isostructural, but α-Al_2O_3 has a significant compressive lattice mismatch to α-Ga_2O_3 of −3.54% along the *c*-axis and −4.81% along the *a*-axis.[32] In >100 nm thick films, this mismatch results in the generation of 10^{10}–10^{11} cm^{-2} threading dislocations during the structural relaxation of α-Ga_2O_3 from the α-Al_2O_3 substrate.[27,32–34] Such high dislocation densities cause the mobility to become dislocation-limited at carrier concentrations of 10^{19} cm^{-3} and lower.[35] For doping at concentrations of $\leq 10^{16}$ cm^{-3}, as are relevant for high-voltage vertical diodes, the dislocation density must be reduced to 10^8 cm^{-3} or lower to prevent the mobility from being dislocation-limited.[35]

Multiple methods have been proposed and utilized for reducing the dislocation densities in α-Ga_2O_3 thin films. The primary method has been growing films thicker and allowing the threading dislocations to recombine.[30] For example, by extending the film thickness from 200 nm to 8 μm, Ma *et al.* were able to decrease the dislocation density from 1×10^{11} to 3×10^9 cm^{-2}.[33] It has also been demonstrated that for the growth of α-Ga_2O_3 by mist CVD on *m*-plane sapphire substrates, higher growth rates lead to reduced quality, but a thin template of higher quality α-Ga_2O_3 grown slowly followed by quickly grown α-Ga_2O_3 results in the entire film being high quality.[30] This suggests that the quality of the nucleation layer at the substrate may be the most important determinant of the overall film quality.

We believe that the key to improving the transport properties of doped α-Ga_2O_3 is lowering the density of dislocations that thread into the layer, either by reducing the number of dislocations that form or increasing the rate at which they recombine in the buffer layer so that fewer propagate into the doped layer. In this

paper, we employ a two-step growth process consisting of a relaxed α-$(Al_xGa_{1-x})_2O_3$ buffer layer with $x = 0.08 \pm 0.02$ grown at high substrate temperature (T_{sub}) to act as a pseudosubstrate. On top of this pseudosubstrate, a Si-doped α-Ga_2O_3 overlayer is grown that is strained to the underlying relaxed buffer layer grown at low T_{sub} to produce a conductive α-Ga_2O_3 layer. The two-step process improves the quality of the nucleation layer and allows us to achieve record high conductivities and mobilities in α-Ga_2O_3 films. We additionally introduce a second, thicker buffer layer in some α-Ga_2O_3 thin films to demonstrate that spacing from the relaxation layer can improve the transport properties.

METHODS

For the growth and doping of α-$(Al_xGa_{1-x})_2O_3$ films by *S*-MBE, we use an elemental aluminum (Alfa Aesar, 6N purity) source, a Ga_2O source formed by mixing liquid gallium (Alfa Aesar, 7N purity) and Ga_2O_3 powder (Alfa Aesar, 5N purity), and a SiO_2 (Kurt J. Lesker, 4N purity) source. The gallium + Ga_2O_3 mixture is made with a 0.4 molecular fraction of oxygen, which thermodynamic calculations conclude will provide a 99.98% pure Ga_2O molecular beam.[36] The Ga_2O mixture is loaded into a custom BeO (Materion Thermalox® CR, 99.7% purity) crucible contained in a Veeco 400 g SUMO® source. The limited purity of the BeO crucible for the Ga_2O source is not a significant concern since the Ga_2O mixture produces a growth flux at relatively low temperatures.[36] Aluminum is loaded into a pyrolytic boron nitride (p-BN) crucible contained in a Veeco 40 cc dual-filament effusion cell. SiO_2 is loaded into a polycrystalline BeO crucible (Materion Thermalox® 995, 99.5% purity) contained in a Veeco 10 cc high-temperature effusion cell. Prior work found that containing SiO_2 in a polycrystalline Al_2O_3 crucible with 99.8% purity led to significant iron contamination being seen in the secondary-ion mass spectrometry (SIMS) of Si-doped β-Ga_2O_3 films, which is a compensating defect in Ga_2O_3.[37] All of the crucibles are loaded into retractable, differentially pumped MBE effusion cells that are mounted on a Veeco Gen10 MBE system. Implementing a 400 g SUMO cell for Ga_2O rather than a 40 cc effusion cell for *S*-MBE is seen to extend the source lifetime and significantly reduces spitting from the source. The smaller opening of the SUMO crucible has led to issues with clogging, but additional tantalum heat shielding and a 100–200 °C tip offset can prevent clogging.

The fluxes of the Ga_2O and aluminum molecular beams are calibrated *in situ* using a quartz crystal microbalance (QCM). The flux of the SiO_2 beam is calibrated by using an Arrhenius fit of fluxes determined by x-ray reflectivity (XRR) measurements on amorphous SiO films deposited onto sapphire substrates held at room temperature in vacuum with the SiO_2 effusion cell at a high temperature of ~1450 °C in combination with a Hall effect measurement of Si-doped homoepitaxial β-Ga_2O_3 grown with the SiO_2 effusion cell at a lower temperature of ~1250 °C.[37] The 10 × 10 mm^2 *m*-plane Al_2O_3 substrates are produced by Kyocera and are oriented with an unintentional miscut of <0.1°. Prior to growth, the substrates are cleaned with Micro-90®, a DI water rinse, acetone, and then isopropanol in a sonicator and annealed in open air at 1000 °C for 5 h. The *m*-plane Al_2O_3 substrates are back-side coated with a 10 nm thick titanium adhesion layer, followed by 200 nm of platinum to enable uniform radiative thermal heating. For reasons that are not yet fully understood, *m*-plane substrates irregularly have a regular step-and-terrace morphology when examined by atomic force microscopy (AFM), which we call "stepped," while most substrates are smooth and featureless, identical to their as-received state, which we call "flat." It has previously been shown that an intentional miscut toward the *a*-direction can support step formation.[38] We believe that the origin of the irregular step formation is our use of well-oriented *m*-plane substrates with no control over the slight (<0.1°) miscut direction. Using intentionally miscut *m*-plane substrates may allow for better control over step formation. Figure S1 of the supplementary material shows AFM images of substrates that demonstrate typical flat [Fig. S1(a)] and stepped [Fig. S1(b)] morphologies. Films G1–G31 were grown on flat substrates, and films G32–G36 were grown on stepped substrates.

The T_{sub} is measured with an optical pyrometer operating at a wavelength of 980 nm. The substrate holders are machined from Haynes® 214® alloy. The aluminum source only has the base filament heated to prevent metal from climbing over the crucible walls and damaging the source.[39] The use of an elemental aluminum source is also motivated by Ellingham diagrams, which show aluminum to readily reduce Ga_2O and form Al_2O, which should readily incorporate into the α-$(Al_xGa_{1-x})_2O_3$ films at the growth conditions used.[40]

The Ga_2O flux (Γ_{Ga_2O}) was fixed at $(5.8 \pm 0.8) \times 10^{14}$ molecules cm^{-2} s^{-1} during the growth of all films for both the unintentionally doped (UID) buffer layers and the Si-doped layers. For the UID α-$(Al_xGa_{1-x})_2O_3$ buffer layers, the aluminum flux (Γ_{Al}) was fixed at $(1.5 \pm 0.5) \times 10^{13}$ atoms cm^{-2} s^{-1}. Except for films G38–G40, the α-$(Al_xGa_{1-x})_2O_3$ buffer layers are (37 ± 2) nm thick and the overlying α-Ga_2O_3 films are 200–700 nm thick. The relatively high T_{sub} (700–800 °C) provides enough thermal energy for the α-Ga_2O_3 or α-$(Al_xGa_{1-x})_2O_3$ buffers to maintain high crystallinity during relaxation and effectively make a pseudosubstrate. Following the UID buffer, an α-Ga_2O_3 layer was deposited at various T_{sub} and background pressures of distilled ozone (~80% O_3 + 20% O_2, $P_{80\%\,O3}$). An effusion cell containing SiO_2 was used to dope the overlying α-Ga_2O_3 layers by supplying an SiO flux.[37,41] The T_{sub} for the Si-doped α-Ga_2O_3 layers ranged from 460–550 °C and $P_{80\%\,O3}$ ranged from 5×10^{-7}–5×10^{-6} Torr. Table I contains the T_{sub}, $P_{80\%\,O3}$, mobile electron carrier concentration measured by Hall effect (n), and the transport properties of every film shown or discussed in this study.

X-ray diffraction (XRD) rocking curves, θ–2θ scans, and XRR measurements were employed at room temperature to characterize the phase purity and structural quality of each sample using a PANalytical Empyrean XRD system utilizing copper $K\alpha_1$ radiation. Rocking curves were measured in a triple-axis configuration using a 220 germanium analyzer crystal. The surfaces of films and substrates were measured by AFM with an Asylum Research Cypher Environmental AFM. The transport properties were determined from Hall effect measurements at 300 K in the van der Pauw geometry using a Nanometrics HL5500 Hall system.

Each sample had indium contacts soldered onto each corner to reduce the contact resistance and enable Hall effect measurements. Select samples had these indium contacts removed with 10 min of soaking in concentrated HCl. These samples then had 10 nm of titanium followed by 110 nm of gold deposited as 1 × 1 mm^2 squares in each corner using electron-beam evaporation with a custom shadow

TABLE I. The growth conditions and resulting transport properties of all α-$(Al_xGa_{1-x})_2O_3$ buffers and α-Ga_2O_3 films in this study. All buffer layers were grown at a pressure of 5 × 10^{-6} Torr. The XRD rocking curve (RC) widths are those of the 300 peak for the overlapping buffer layer and α-Ga_2O_3 film. The listed n, μ, and σ are the values determined by Hall effect measurements. For electrically insulating samples, we list the expected donor concentration, N_D.

ID	$T_{sub,Buffer}$ (°C)	$T_{sub,Film}$ (°C)	$P_{80\%O3,film}$ (Torr)	300 RC FWHM (arc sec)	n (cm^{-3})	σ (S/cm)	μ (cm^2/V s)	Contact-type
G1	N/A	480	5×10^{-6}	Amorphous	Insulating ($N_D = 6.6 \times 10^{19}$)	⋯	⋯	In
G2	700	540	1×10^{-6}	970	Insulating ($N_D = 2.3 \times 10^{18}$)	⋯	⋯	In
G3	750	480	5×10^{-6}	1020	4.2×10^{19}	420	62	In
G4	750	480	1×10^{-6}	890	4.3×10^{19}	390	55	In
G5	750	480	5×10^{-6}	600	4.2×10^{19}	540	79	In
G6	750	500	1×10^{-6}	990	2.8×10^{19}	77	17	Ti/Au
G7	750	525	1×10^{-6}	960	Insulating ($N_D = 1.1 \times 10^{20}$)	⋯	⋯	Ti/Au
G8	750	550	1×10^{-6}	1000	Insulating ($N_{Si} = 3.9 \times 10^{20}$)	⋯	⋯	Ti/Au
G9	750	460	5×10^{-6}	660	4.8×10^{19}	570	73	In
G10	750	470	5×10^{-6}	720	4.2×10^{19}	510	74	In
G11	700	550	5×10^{-6}	1020	Insulating ($N_D = 9.9 \times 10^{18}$)	⋯	⋯	In
G12	750	550	5×10^{-6}	870	1.8×10^{18}	4.4	15	In
G13	700	550	1×10^{-6}	890	Insulating ($N_D = 1.1 \times 10^{19}$)	⋯	⋯	Ti/Au
G14	700	550	5×10^{-7}	830	Insulating ($N_D = 1.4 \times 10^{19}$)	⋯	⋯	Ti/Au
G15	750	500	5×10^{-7}	1010	Insulating ($N_D = 1.0 \times 10^{19}$)	⋯	⋯	In
G16	750	480	5×10^{-6}	670	4.9×10^{19}	650	82	In
G17	750	480	5×10^{-6}	820	1.9×10^{19}	170	54	In
G18	750	480	5×10^{-6}	810	4.2×10^{19}	320	73	In
G19	750	480	5×10^{-6}	800	5.3×10^{18}	72	53	In
G20	750	500	2×10^{-6}	880	3.5×10^{18}	64	68	In
G21	725	550	5×10^{-6}	1010	Insulating ($N_D = 1.5 \times 10^{19}$)	⋯	⋯	In
G22	750	500	5×10^{-6}	800	3.0×10^{19}	320	67	Ti/Au
G23	750	500	5×10^{-6}	760	2.4×10^{19}	190	49	Ti/Au
G24	750	500	5×10^{-6}	870	2.0×10^{19}	200	71	In
G25	750	500	5×10^{-6}	830	1.2×10^{19}	130	71	Ti/Au
G26	750	500	5×10^{-6}	840	6.4×10^{18}	67	64	Ti/Au
G27	750	500	5×10^{-6}	830	2.2×10^{18}	29	79	Ti/Au
G28	750	500	5×10^{-6}	810	9.9×10^{17}	7.6	51	Ti/Au
G29	750	500	5×10^{-6}	830	4.2×10^{17}	2.2	31	Ti/Au
G30	750	500	5×10^{-6}	820	Insulating ($N_D = 3.2 \times 10^{17}$)	⋯	⋯	Ti/Au
G31	800	540	1×10^{-6}	930	3.7×10^{18}	16	26	Ti/Au
G32	730	425	1×10^{-6}	1510	2.0×10^{19}	57	20	In
G33	730	480	1×10^{-6}	1270	1.1×10^{19}	67	40	In
G34	800	540	1×10^{-6}	1270	1.1×10^{19}	140	79	In
G35	800	570	1×10^{-6}	1290	7.9×10^{18}	14	11	In
G36	800	600	1×10^{-6}	1290	Insulating ($N_D = 3.0 \times 10^{19}$)	⋯	⋯	In
G37	725, 550	500	2×10^{-6}	1100	2.9×10^{19}	420	90	In

mask made of alloy 316 stainless steel. Samples with Ti/Au contacts and carrier concentrations below 10^{19} cm^{-3} had highly Si-doped (5×10^{19} cm^{-3}) α-Ga_2O_3 1 × 1 mm^2 triangular contacts regrown onto the corners with *S*-MBE before the Ti/Au contacts were applied. The highly Si-doped regrown contacts were grown using a sapphire shadow mask for 10 min at $P_{80\%O3} = 5 \times 10^{-6}$ Torr and T_{sub} = 490 °C, resulting in a thickness of ~100 nm. Following the deposition of the Ti/Au contacts, the samples were annealed at 500 °C in a flowing N_2 atmosphere for 2 min. Figure S3 of the supplementary material shows *I*–*V* curves of sample G27 after multiple annealing temperatures, with 500 °C being the optimal annealing temperature. Our annealing recipe is similar to previous results that found Ti/Au to form ohmic contacts with minimal R_c on α-Ga_2O_3 after a 450 °C anneal.[42] Table I lists whether each film had indium contacts or Ti/Au contacts for the Hall effect measurement.

Scanning transmission electron microscopy (STEM) was used to confirm the density of threading dislocations in sample G5.

A cross-section lamella was prepared using the Thermo Fisher Helios G4 UX Focused Ion Beam. Protective amorphous carbon and platinum layers were deposited onto the lamella and prepared with a final milling step of 2 keV to reduce damage. The STEM measurements were taken with an aberration-corrected Thermo Fisher Spectra 300 CFEG operated at 300 keV. The density of threading dislocations was also estimated for film G5 by measuring rocking curves on one symmetric peak and multiple asymmetric peaks and fitting the FWHM as a function of the inclination angle of each reflection. This method has previously been demonstrated to match well with STEM measurements for α-Ga_2O_3 films grown on *c*-plane sapphire.[33] The Burgers vectors for edge dislocations and screw dislocations of α-Ga_2O_3 on *m*-plane sapphire are taken to be $b_e = \langle 110 \rangle$ and $b_s = \frac{1}{3}\langle 1\bar{1}0 \rangle$ for *m*-plane α-Ga_2O_3, which have magnitudes of 4.98 and 2.88 Å, respectively.[34]

SIMS measurements were made on samples G6, G8, G16, G23, G25, G26, G29, G30, and G37 using a Hiden Analytical SIMS Plus Workstation. The Hiden system used an O_2^+ ion source as the primary beam to profile the sample with a voltage and current for the analysis of 2 kV and 50 nA, respectively. The O_2^+ primary ion beam was oriented at 45° relative to the sample surface, while a MAXIM quadrupole mass analyzer was angled at 30° to the probe axis. The crater area, scan density, electronic gating, system base pressure, and the pressure during profiling were 500 × 500 μm^2, 100 × 100 pixel^2, 10% of the raster area, 5.0×10^{-10} Torr, and 2.0×10^{-8} Torr, respectively.

Prior to the SIMS measurements that are shown in this manuscript, two α-Ga_2O_3 films were grown to create SIMS standards. The first of these undoped films consisted of two α-Ga_2O_3 layers that were grown at T_{sub} = 725 °C and $P_{80\%\,O3} = 5 \times 10^{-6}$ Torr and 550 °C and $P_{80\%\,O3} = 1 \times 10^{-6}$ Torr on flat *m*-plane Al_2O_3 substates, with a total thickness of 670 nm. The second undoped film was composed of two α-Ga_2O_3 layers that were grown at T_{sub} = 725 °C and $P_{80\%\,O3} = 5 \times 10^{-6}$ Torr and 575 °C and $P_{80\%\,O3} = 1 \times 10^{-6}$ Torr on flat *m*-plane Al_2O_3 substates, with a total thickness of 480 nm. Both samples were implanted with 10^{14} cm^{-2} doses of boron, beryllium, silicon, and iron by CuttingEdge Ions©. These calibration standards in combination with the depth of the SIMS crater measured by profilometry, allowed the measured SIMS intensities to be converted to elemental concentrations.

The optical bandgaps, E_g, of films G22–G30 were measured using ellipsometry to confirm phase purity, as α-Ga_2O_3 has the highest optical bandgap of all Ga_2O_3 phases. All 16 Mueller elements for the films were collected using a JA Woolam RC2 ellipsometer for azimuthal angles 0° (along the optical axis) and 90° (orthogonal to the optical axis) for photon energies in the range of 0.73–6.42 eV with a resolution of 0.03 eV. The angles of incidence varied from 45° to 75° in 5° steps. An initial anisotropic B-Spline model for the α-$(Al_xGa_{1-x})_2O_3$ buffer layer on *m*-plane α-Al_2O_3 was developed with a thickness of (37 ± 2) nm determined by XRR and a composition of $x = 0.08 \pm 0.02$ determined by the 2θ peak position in the θ–2θ XRD scan. This film was a model of the buffer that was used in all films G2–G36, unless otherwise specified. The α-$(Al_{0.08}Ga_{0.92})_2O_3$ model was used in the subsequent ellipsometry analysis. To further estimate the thickness and roughness of the α-Ga_2O_3 films, an initial anisotropic fit using a Cauchy model in difference mode $[(n_0(\hbar\omega) - n_e(\hbar\omega))|_{\hbar\omega<3eV} = 0.02]$, where n_0 and n_e are the ordinary and extraordinary indices of refraction at photon energy $\hbar\omega$, respectively, was done in the transparent region (<3 eV).[43] These values were fixed for the subsequent analysis. The dielectric function was modeled with two Kramers–Kronig enforced B-Spline layers with a node spacing of 0.03 eV, which were simultaneously fit for the two azimuthal angles. From the dielectric function, we write the corresponding absorption coefficient $\alpha(\hbar\omega) = \frac{4\pi Im\left(\sqrt{\varepsilon(\hbar\omega)}\right)}{\lambda}$, where ε is the permittivity and λ is the wavelength. The absorption coefficient was then used to extract the Tauc bandgap of the material using a Tauc-plot fit of $E_g \propto (\hbar\omega\alpha)^2$ for both the ordinary and the extraordinary dielectric functions. We observe that the bandgap along the extraordinary direction is larger than along the ordinary direction. We report the ordinary bandgap from the Tauc fitting as the optical bandgap of the material.

RESULTS AND DISCUSSION

The θ–2θ XRD scans of samples G1–G5 are compared in Fig. 1 to determine whether the implementation of a high-temperature relaxed α-Ga_2O_3 or a relaxed α-$(Al_xGa_{1-x})_2O_3$ buffer layer can template the low-temperature growth of α-Ga_2O_3. Each sample was grown with different buffer layer conditions to determine which works best. G1 is used as a control sample with no buffer layer; only an Si-doped α-Ga_2O_3 film is grown. G2 and G3 have α-Ga_2O_3 buffer layers, while G4 and G5 have α-$(Al_xGa_{1-x})_2O_3$ buffers with $x = 0.08 \pm 0.02$. Figure S2 of the supplementary material shows the θ–2θ scan of an example α-$(Al_{0.08}Ga_{0.92})_2O_3$ buffer layer and confirms that the α-$(Al_{0.08}Ga_{0.92})_2O_3$ buffer is relaxed from the α-Al_2O_3 substrate. The example α-$(Al_{0.08}Ga_{0.92})_2O_3$ buffer shown in Fig. S2 was grown for 10 min at $P_{80\%\,O3} = 5 \times 10^{-6}$ Torr and T_{sub} = 750 °C. The α-$(Al_xGa_{1-x})_2O_3$ buffer must have low aluminum content so that the Si-doped α-Ga_2O_3 layer grown upon it does not relax from the buffer layer, which would introduce additional threading dislocations. G2 and G4 have their Si-doped layers grown at $P_{80\%\,O3} = 1 \times 10^{-6}$ Torr, while G3 and G5 have their Si-doped layers grown at $P_{80\%\,O3} = 5 \times 10^{-6}$ Torr. The growth conditions for all films and buffers, as well as their resulting transport properties, are listed in Table I.

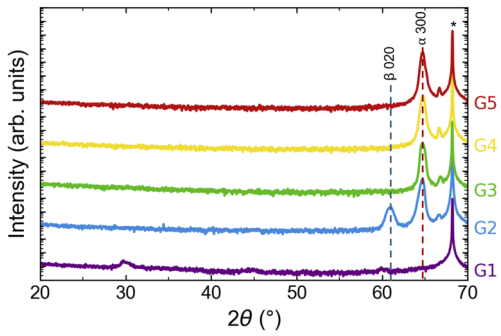

FIG. 1. θ–2θ XRD scans of samples G1–G5 over the 2θ = 20°–70° range, offset along the vertical intensity axis for clarity. The 300 peak of the α-Al_2O_3 substrate is marked by the * symbol, and the 300 α-Ga_2O_3 and 020 β-Ga_2O_3 reflections are labeled above the dashed red and dashed blue lines, respectively. The broad, weak peaks at 30° and 44° seen only in G1 are believed to be κ–Ga_2O_3 impurity phase peaks.

The results in Fig. 1 confirm that the high-temperature buffer is necessary for substantial overgrowth of phase-pure epitaxial α-Ga_2O_3 since G1 has weak and broad peaks, suggesting limited crystalline growth with low crystalline quality and at least one impurity phase present without a buffer layer. The peaks at 30° and 44° in the θ–2θ scan of G1 are consistent with κ-Ga_2O_3 inclusions, and the peak at 60° signals 020 β-Ga_2O_3 formation. With no aluminum in the buffer layer and low $P_{80\%\,O3}$ during doping, sample G2 exhibits no measurable conductivity and shows the formation of the β-Ga_2O_3 inclusions. In contrast, G3–G5 all show phase-pure epitaxial α-Ga_2O_3 growth with substantial peak intensity, supporting our hypothesis that a relaxed high-temperature buffer layer could act as a pseudosubstrate and template the growth of phase-pure α-Ga_2O_3 at low T_{sub}. The additional peak at 66.9° in the θ–2θ scans of G2–G5 is believed to be a hybrid reflection formed by the 200 substrate plus 100 film reflections, which is supported by Fig. S4 of the supplementary material.[44] In Fig. S4(a) of the supplementary material, the 300 α-Ga_2O_3 and the 300 α-Al_2O_3 peaks appear in both scans with little change in intensity and position, as expected for symmetric peaks. In the $\Phi = -2.5°$ scan, an extra peak appears at 66.9°, which is within 0.15° of the calculated position for the 200 substrate plus 100 film hybrid reflection, $2\theta = 67.04°$. The extreme sensitivity to Φ and agreement with the calculated reflection position are consistent with the peak being a hybrid reflection.[44] By changing Φ after aligning to the 300 α-Al_2O_3 substrate peak, we are consistently able to get this 200 substrate plus 100 film hybrid reflection to appear. These peaks appear in all films grown with buffer layers and do not appear in films without buffer layers. Figure S4(b) shows that the film and substrate Φ scans have intense reflections at all values of Φ, which is consistent with symmetric film reflections, while the suspected hybrid reflection shows four narrow, sharp peaks in Φ, which is consistent with hybrid reflections.

Of the samples shown in Fig. 1, only samples G3, G4, and G5 are conductive. In contrast to sample G2, the Si-doped layer of sample G3 was grown at a higher $P_{80\%\,O3}$ and remains phase pure with a conductivity of 422 S/cm. The Si-doped layer of G2 was grown at $T_{sub=}$540 °C rather than T_{sub} = 480 °C at which all the other Si-doped layers of the samples in Fig. 1 were grown, which may also contribute to the lack of conductivity. The difference between G2 and G3 suggests that β-Ga_2O_3 formation and poor transport may be issues for films grown in low $P_{80\%\,O3}$ and high T_{sub} conditions, even with α-Ga_2O_3 buffer layers. In contrast to G2 and G3, samples G4 and G5 had aluminum added to their buffer layers and both remained phase-pure. Additionally, samples G4 and G5 have relatively high conductivities of 387 S/cm and 544 S/cm, respectively. The FWHM of the 300 rocking curve of the Si-doped α-Ga_2O_3 layer also decreases from 970 to 890 arc sec with the α-$(Al_xGa_{1-x})_2O_3$ buffer, suggesting that the structural quality improves when aluminum is added to the buffer layer. The addition of aluminum to the buffer also improves transport in high $P_{80\%\,O3}$ conditions, which can be seen by G5 having higher conductivity than G3. The improved structural quality offered by the α-$(Al_xGa_{1-x})_2O_3$ buffer is corroborated as the 300 rocking curve FWHM of the Si-doped α-Ga_2O_3 layer improves from 1020 arc sec for G3 to 600 arc sec for G5. Comparing G2–G4 and G3–G5, the α-$(Al_xGa_{1-x})_2O_3$ buffer successfully prevents β-Ga_2O_3 inclusions and leads to higher conductivity. Additionally, increasing $P_{80\%\,O3}$ to 5×10^{-6} Torr during growth and doping leads to both G3 and G5 being more conductive than G2 and G4.

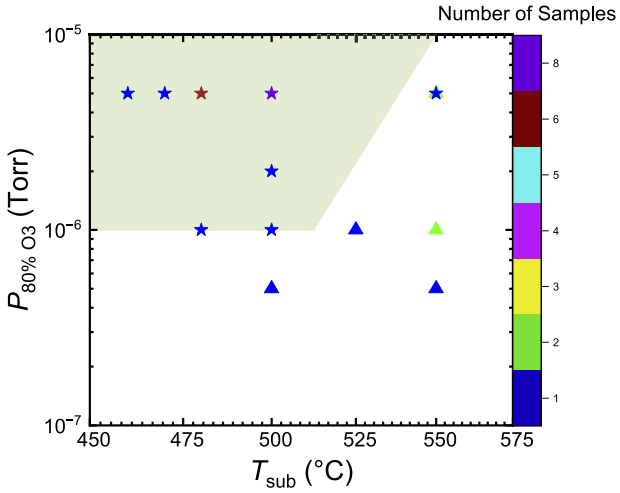

FIG. 2. A $P_{80\%\,O3}$ - T_{sub} map showing the growth conditions resulting in conductive films, marked by stars, and insulating films, marked by triangles. In the figure, the minimum conductivity for a sample to be considered conductive is 1 S/cm. The color of each point disambiguates how many samples were grown in identical conditions. The light green region marks the growth conditions where all films turned out conductive.

Overall, Fig. 1 confirms that a buffer is necessary for the growth of conductive α-Ga_2O_3 at low T_{sub} and that adding aluminum to the buffer can further improve the structural quality, while higher $P_{80\%\,O3}$ values may improve the transport properties.

Next, to determine which growth conditions are most favorable for growing conductive α-Ga_2O_3 with *S*-MBE, samples G3–G28 were grown over the range of $P_{80\%\,O3} = 5 \times 10^{-7}$–$5 \times 10^{-6}$ Torr and T_{sub} = 460–550 °C and are compared in Fig. 2. We see that our α-Ga_2O_3 films are always electrically insulating if grown at a $P_{80\%\,O3} < 1 \times 10^{-6}$ Torr. We similarly find that Si-doped α-Ga_2O_3 films grown at $T_{sub} > 550$ °C are never conductive, while Si-doped α-Ga_2O_3 films grown at $500 < T_{sub} < 550$ °C are inconsistently conductive but only at relatively high $P_{80\%\,O3}$. Specifically, only one of the three films grown at $T_{sub} = 550$ °C and $P_{80\%\,O3} = 5 \times 10^{-6}$ Torr is conductive, suggesting that $T_{sub} \leq 500$ °C is still preferable even at high $P_{80\%\,O3}$. This is believed to be either a result of lower $P_{80\%\,O3}$ and higher T_{sub} conditions, which increases the surface lifetime of adatoms and the chance of the donor, Si^{4+}, reaching a dislocation and being compensated, or of the donor failing to find an oxygen adatom and incorporating as SiO, thereby behaving as an acceptor.[17,26,30]

The green region of Fig. 2 marks the most optimal conditions for the growth and Si-doping of conductive α-Ga_2O_3 by *S*-MBE. For the most ideal growth conditions, $T_{sub} \leq 500$ °C and $P_{80\%\,O3} \geq 1 \times 10^{-6}$ Torr, the growth of conductive α-Ga_2O_3 is highly reproducible, and all 19 Si-doped α-Ga_2O_3 thin films are conductive. G30 is excluded from the figure because it is expected to have $n \leq 1 \times 10^{17}$ cm^{-3}, and forming ohmic contacts remains challenging. G30 is insulating by both 2-point multimeter readings and Hall effect measurements. If this sample was included, 19 of 20 samples in the green region would be considered conductive. The requirement of low T_{sub} for conductivity supports the previous finding that

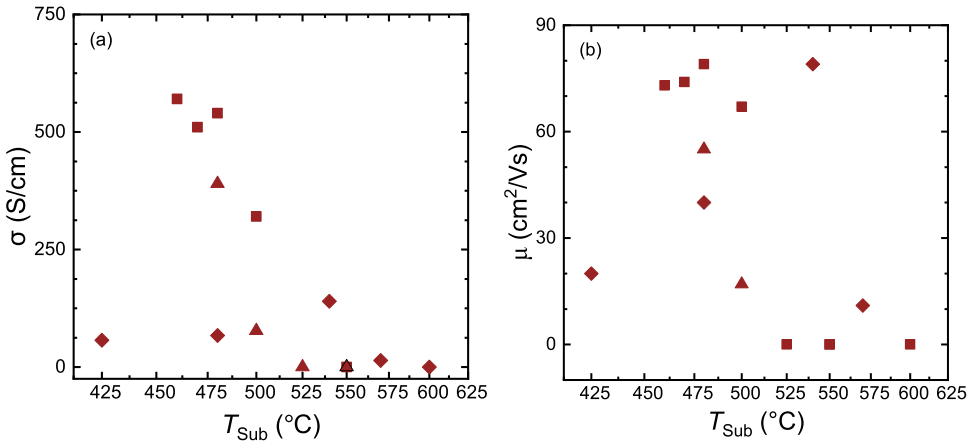

FIG. 3. (a). A comparison of the conductivity of α-Ga_2O_3 thin films as a function of the substrate temperature at which the Si-doped layer was grown. (b) A plot of the mobility of α-Ga_2O_3 thin films as a function of T_{sub}. The samples with $P_{80\%\,O3}$ = 1 × 10^{-6} Torr have a target n of (9.0 ± 2.5) × 10^{19} cm^{-3}, while the samples with $P_{80\%\,O3}$ = 5 × 10^{-6} Torr have a target n_e of (6.20 ± 0.15) × 10^{19} cm^{-3}. The films grown on stepped substrates have a target n of (1.85 ± 0.25) × 10^{19} cm^{-3}. Triangle markers represent samples grown on "flat" substrates with $P_{80\%\,O3}$ = 1 × 10^{-6} Torr, square markers represent samples grown on "flat" substrates at $P_{80\%\,O3}$ = 5 × 10^{-6} Torr, and diamond markers represent samples grown on "stepped" substrates.

a relaxed buffer layer with good crystalline quality is necessary for the growth of an overlying conductive doped α-Ga_2O_3 film since growth and doping of α-Ga_2O_3 at low T_{sub} is only possible with a pseudosubstrate template.[17,26,30]

Next, to find the growth conditions for *S*-MBE that result in the best transport properties, the conductivity and mobility of samples G4–G11, G22, and G32–G36 are plotted as a function of T_{sub} and $P_{80\%\,O3}$ in Fig. 3. The samples grown at $P_{80\%\,O3}$ = 5 × 10^{-6} Torr have a target donor concentration of N_D = (6.20 ± 0.15) × 10^{19} cm^{-3}, and samples grown at $P_{80\%\,O3}$ = 1 × 10^{-6} Torr have target N_D = (9.0 ± 2.5) × 10^{19} cm^{-3}. The films grown on stepped substrates have N_D = (1.85 ± 0.25) × 10^{19} cm^{-3}. Consistent with the findings of Fig. 2, conductivity is only observed in the films grown at T_{sub} ≤ 500 °C. The mobility and conductivity are higher for the higher $P_{80\%\,O3}$ samples at all T_{sub} values, again consistent with the findings of Fig. 2. The specific growth conditions and transport properties of each film are given in Table I.

Samples G32–G36 were grown on stepped substrates rather than the flat substrates used throughout the rest of this paper. The comparison in Fig. 3 primarily shows that the growth of α-Ga_2O_3 on stepped substrates is seen to result in reduced σ and μ compared to flat substrates at the same mobile carrier concentration, n, especially at T_{sub} ≤ 500 °C, where flat substrates produce α-Ga_2O_3 films with the best transport properties. The lower σ values may result from the lower target N_D for the films on stepped substrates. A lower N_D is expected to result in higher Hall mobilities, which is not observed across the majority of tested T_{sub}. This suggests that the lower σ and μ values are due to the reduced crystalline perfection of the α-Ga_2O_3 films.

Our results show that conductive α-Ga_2O_3 thin films can be grown at T_{sub} as low as 425 °C on stepped substrates, which is back-end-of-line (BEOL) compatible. This is in agreement with prior reports that α-Ga_2O_3 is the widest bandgap semiconductor that can be deposited in BEOL conditions, but our mobilities under BEOL conditions are nearly 100 times higher.[45,46] This growth in BEOL conditions requires a α-Ga_2O_3 buffer, which is grown at high T_{sub} in *S*-MBE and cannot be done fully in BEOL conditions. It may be possible to grow the initial relaxed α-Ga_2O_3 buffer with ALD or mist CVD, both of which have demonstrated growth of α-Ga_2O_3 in BEOL conditions, followed by highly conductive α-Ga_2O_3 grown by *S*-MBE.[45,46] Similar conditions have not been tested for flat substrates, but the advantage in transport properties from T_{sub} = 460–500 °C suggests that BEOL temperatures may result in better films on flat substrates. One potential advantage offered by the stepped substrates is that exclusively in the temperature range of T_{sub} > 500 °C, the mobility is higher than on the flat substrates at the same n. A possible explanation for this is that the step-and-terrace morphology may enable 2D step-flow growth, which requires increased T_{sub}.[47]

With the ideal range of $P_{80\%\,O3}$ and T_{sub} for the growth and doping of α-Ga_2O_3 by *S*-MBE determined in Figs. 2 and 3, we selected $P_{80\%\,O3}$ = 5 × 10^{-6} Torr and T_{sub} = 500 °C as the conditions for a doping series. All films in this series have α-$(Al_xGa_{1-x})_2O_3$ buffer layers with x = 0.08 ± 0.02 that are approximately (37 ± 2) nm thick and overlying Si-doped α-Ga_2O_3 layers with thicknesses in the range of (415 ± 55) nm. The target n_e for the films in this series ranged from 3.2 × 10^{17}–9.8 × 10^{19} cm^{-3}. The resulting mobilities and conductivities are plotted as a function of the mobile carrier concentration determined by Hall effect measurements in Fig. 4. The samples in Fig. 4 are G22–G30, and the growth conditions and resulting transport properties for each film are listed in Table I. The goal of this series was to determine at what carrier concentration dislocation scattering began to dominate, which defines the range of carrier concentrations that can be grown effectively.

In Fig. 4, the peak mobility in our α-Ga_2O_3 films occurs for a carrier concentration of 3 × 10^{19} cm^{-3}, and the transition to

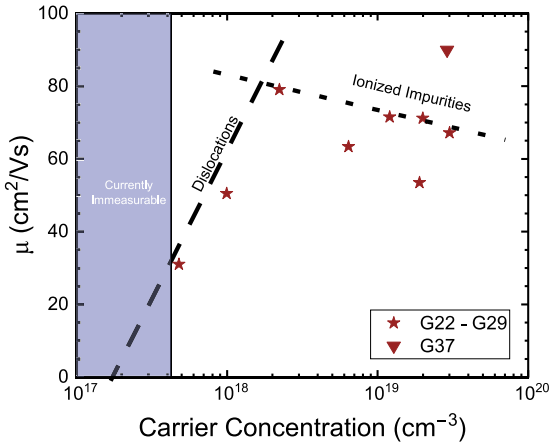

FIG. 4. A plot of the mobility and conductivity of films G22–G29 and G37 as a function of their measured carrier concentration. The values for μ, σ, and n come from Hall effect measurements. The films marked with a star in this plot are all grown with $P_{80\%\,O3} = 5 \times 10^{-6}$ Torr and $T_{sub} = 500\,^{\circ}C$ as the growth conditions for the Si-doped α-Ga_2O_3 overlayers and $P_{80\%\,O3} = 5 \times 10^{-6}$ Torr and $T_{sub} = 750\,^{\circ}C$ as the growth conditions for the UID α-$(Al_xGa_{1-x})_2O_3$ buffer layers. The Si-doped α-Ga_2O_3 overlayers for the samples marked by stars have thicknesses of 415 ± 55 nm, and the buffer layers are approximately (37 ± 2) nm thick. The sample marked with a triangle, G37, has an initial buffer layer grown at $P_{80\%\,O3} = 5 \times 10^{-6}$ Torr and $T_{sub} = 550\,^{\circ}C$ that is ~50 nm thick and an additional UID buffer layer that is grown at $P_{80\%\,O3} = 5 \times 10^{-6}$ Torr and $T_{sub} = 550\,^{\circ}C$ that is ~310 nm thick. The dashed line represents the region of dislocation-limited μ as a function of n, and the dotted line represents the region of ionized-impurity scattering limited μ as a function of n, for samples G22–G29.

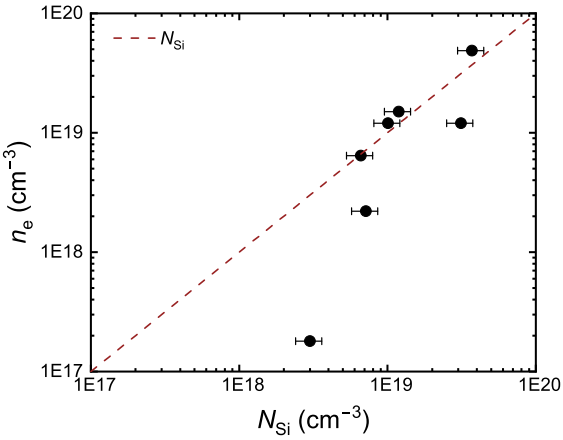

FIG. 5. A plot of n_e, determined by Hall measurements, as a function of the concentration of silicon atoms, N_{Si}, determined by SIMS measurements. Error bars of ±20% in the SIMS measured N_{Si} are included for each data point.[48,49] The dashed line shows the expected trend of n_e as a function of N_{Si} if 100% of the incorporated Si donors are electrically active.

dislocation-limited mobility occurs around 2×10^{18} cm^{-3}. At high carrier concentrations, the expected decrease in mobility due to increased ionized-impurity scattering occurs. Below a carrier concentration of 2×10^{18} cm^{-3}, the mobility plummets as the mobile carrier concentration falls, as the dominant scattering mechanism changes from ionized-impurity scattering to dislocation scattering. This occurs because the concentration of ionized impurities decreases and screens the dislocation scattering less, increasingly allowing dislocation scattering to limit the mobility. For homoepitaxial films of other semiconductors, e.g., β-Ga_2O_3, the dislocation densities are many orders of magnitude lower, so the concentration where dislocations begin to dominate is extremely low. Metastable systems, such as α-Ga_2O_3, however, often require heteroepitaxy since they cannot be stabilized as bulk substrates to enable homoepitaxy. The significant lattice mismatch and strain involved in the heteroepitaxial growth of α-Ga_2O_3 on sapphire results in a relatively high concentration of 10^{10}–10^{11} cm^{-2} threading dislocations upon relaxation, causing the mobility to be primarily limited by dislocation scattering at carrier concentrations as high as 2×10^{18} cm^{-3}, which is consistent with Fig. 5.[27,32–35]

In Fig. 5, the active carrier concentration, n_e, is plotted as a function of the SIMS determined donor concentration, N_{Si}, to extract the activation ratio of donors in films G6, G8, G16, G23, G25, G27, G29, G30, and G37. The fit of n_e as a function of N_{Si} is the activation ratio of the incorporated silicon and is plotted against the dashed line in Fig. 5, which represents full incorporation of the supplied flux, N_{Si}. The error bars on the measured value of N_{Si} by SIMS are typical of the technique and account for ~±20% error.[48,49] The SIMS measurement of sample G23 is shown as an example in Fig. S5(a) of the supplementary material. Clear interfaces between the film, buffer, and substrate are seen in the SIMS spectra and show that the silicon concentration is relatively constant throughout the doped layer. The activation rate of silicon donors at $N_{Si} \gtrsim 10^{19}$ cm^{-3} is ~100%. At lower values of N_{Si}, below 10^{18} cm^{-3}, the effective activation ratio rapidly falls to 0. This is expected to be a result of threading dislocations acting as Read cylinders that remove an approximately constant concentration of carriers.[50,51] This reduces the effective activation of low N_{Si} samples by removing a larger fraction of the active carriers and results in a minimum N_{Si} where active carriers can be observed. This leads to a limited range within which the doping can be effectively controlled of ~$10^{18} \leq n_e \leq 10^{20}$ cm^{-3}. To broaden the range of effective doping, reducing the threading dislocation density is necessary to limit the number of carriers that are lost.

SIMS was also measured on film G8 to investigate why the films grown outside of the ideal growth conditions found in Fig. 3 are electronically insulating. The SIMS of film G8 is shown in Fig. S6 (b) of the supplementary material. Similar to the SIMS of sample G23, clear interfaces between the film, buffer, and substrate are seen. The Si concentration is also consistent throughout the doped layer at a value of $N_{Si} = 3.9 \times 10^{19}$ cm^{-3}. This shows that even in films that are electrically insulating, such as G8, Si is readily incorporated but is not active. Since the insulating films have rocking curves with similar FWHM to the conductive films, the complete deactivation cannot be fully due to Read cylinders. Several hypotheses could explain this behavior. One is that when incorporated at elevated T_{sub}, significant concentrations of Si incorporate in the 2+ oxidation state and act as compensating defects.[26] Another is that at elevated T_{sub}, the silicon dopant has a longer diffusion length and enough thermal energy to diffuse to and get pinned at a dislocation, where it forms a Cottrell atmosphere.[52] Such dopant pinning

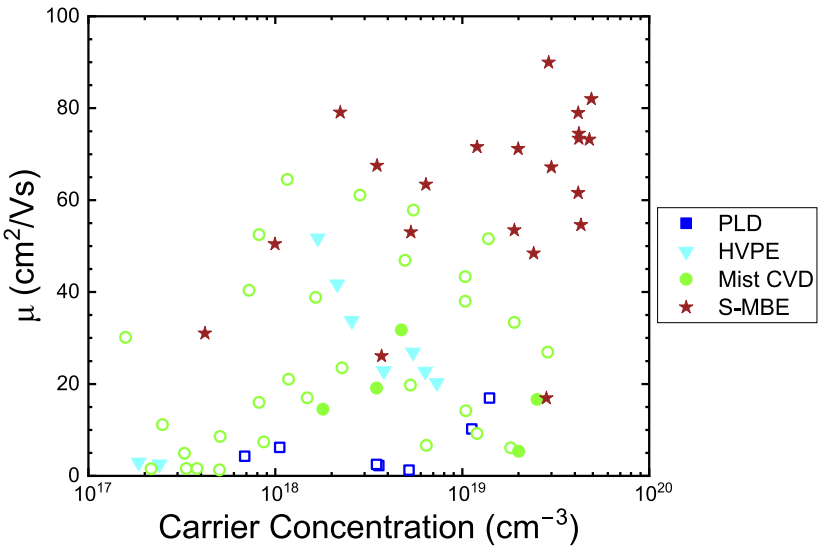

FIG. 6. A comparison of the mobilities of Si- and Sn-doped α-Ga_2O_3 grown by PLD (squares),[26] HVPE (triangles),[15] mist CVD (circles),[30] and *S*-MBE (stars, this work) as a function of mobile carrier concentration. Solid markers represent films grown with silicon doping, and empty markers represent films with tin doping. The Si-doped α-Ga_2O_3 films in this study have mobilities higher than all other reports at $n \geq 2.2 \times 10^{18}$ cm^{-3}.

at dislocations (and deactivation because of the percent-level high concentrations commonly observed in Cottrell atmospheres) has been seen in As-doped silicon, B-doped silicon, and Mg-doped GaN.[53–55]

In Fig. 6, we compare the mobilities of our Si-doped α-Ga_2O_3 films to previous α-Ga_2O_3 studies in which conducting Sn- or Si-doped α-Ga_2O_3 films were grown by PLD,[26] HVPE,[14] or mist CVD.[17,18,30] The films grown by *S*-MBE show a range of active doping, from 4.2×10^{17} to 4.8×10^{19} cm^{-3}, reaching the highest mobile carrier concentration of any study to date. Our α-Ga_2O_3 samples grown by *S*-MBE with carrier concentrations $\geq 2.2 \times 10^{18}$ cm^{-3} also demonstrate the highest reported mobilities of any study. Twelve of the films shown in this study exceed the previous record of μ = 65 $\frac{cm^2}{V \cdot s}$ set by tin doping with mist CVD.[30] The maximum mobility in this set is μ = 90 $\frac{cm^2}{V \cdot s}$, which occurs at a carrier concentration of 2.9×10^{19} cm^{-3}. The mobility before the transition to the dislocation-limited regime occurs is 79 $\frac{cm^2}{V \cdot s}$ at a carrier concentration of 2.2×10^{18} cm^{-3}. This transition point is comparable to the transition point for Sn-doped α-Ga_2O_3 grown by mist CVD.[30] Since the impurity concentrations in mist CVD are high, over 10^{18} cm^{-3}, the transition to dislocation scattering is screened by the additional impurities, which suppresses the transition to the regime where the mobility is limited by dislocation scattering.[30] We believe that the record-setting transport properties that we observe are primarily a result of the lower chemical impurity concentrations and donor activation possible with MBE growth. A second reason for the comparably high mobilities could be the superior structural quality of α-Ga_2O_3 films grown by *S*-MBE. This is supported by an average symmetric rocking curve FWHM of 834 arc sec, which is nearly 20% lower than the previous record of ~1000 arc sec for doped α-Ga_2O_3 grown on *m*-plane sapphire.[16] As the FWHM of rocking curves increases with the mosaicity of the films, narrower rocking curves are correlated with reduced threading dislocation densities and dislocation scattering.

To better understand the record transport behavior of α-Ga_2O_3 films grown by *S*-MBE, we grew a set of α-Ga_2O_3 films at 500 °C on top of α-$(Al_xGa_{1-x})_2O_3$ buffer layers with varied target doping levels ranging from 3.2×10^{17} to 9.8×10^{19} cm^{-3}. In Fig. S8 of the supplementary material, the ordinary E_g of this set of α-Ga_2O_3 films G22–G28 determined by ellipsometry is compared to the measured mobile carrier density, *n*, or the target donor concentration, N_D. All films have bandgaps of 5.36 eV or higher, which confirms the phase purity of the α-Ga_2O_3 films, as all other phases of Ga_2O_3 have lower bandgaps. The trend of mobility vs *n* for the sample set shows the expected transition from where mobility is limited by ionized impurity scattering to where it is limited by dislocation scattering. The transition between these two scattering-limited mobility regimes is seen to occur at a carrier concentration of 2.2×10^{18} cm^{-3}, which is comparable to the value seen in prior studies and suggests similar threading dislocation densities.

To estimate the dislocation density with XRD measurements, we fit a plot of the FWHM of skew-symmetric rocking curves as a function of inclination angle in Fig. S6(b) of the supplementary material.[33,34] This fitting procedure assumes that the out-of-plane tilt broadening comes completely from screw dislocations and the in-plane twist broadening comes entirely from edge dislocations. For the estimation, we measured the rocking curves of the 300, 220, 104, 113, 01$\bar{4}$, and 2$\bar{2}$4 reflections of film G5, which are shown in Fig. S6(a) in the supplementary material. The rocking curves are shown in Fig. S6(a), with their intensities scaled to the same value for clarity. This is the film that is measured with STEM to determine the true density of threading dislocations in Fig. 7. The FWHM for the rocking curves of the 300, 220, 104, 113 01$\bar{4}$, and 2$\bar{2}$4 reflections of film G5 are found to be 0.167°, 0.359°, 0.285°, 0.264°, 0.403°, and 0.357°, respectively. The inclination angles for the 300, 220, 104, 113, 01$\bar{4}$, and 2$\bar{2}$4 reflections are 0°, 30°, 40.5°, 51.8°, 65°, and 72°, respectively, for α-Ga_2O_3.

The fit of film G5 in Fig. S6(b) of the supplementary material gives $K_{twist} = 0.39° \pm 0.04°$ and $K_{tilt} = 0.20° \pm 0.06°$. The edge and

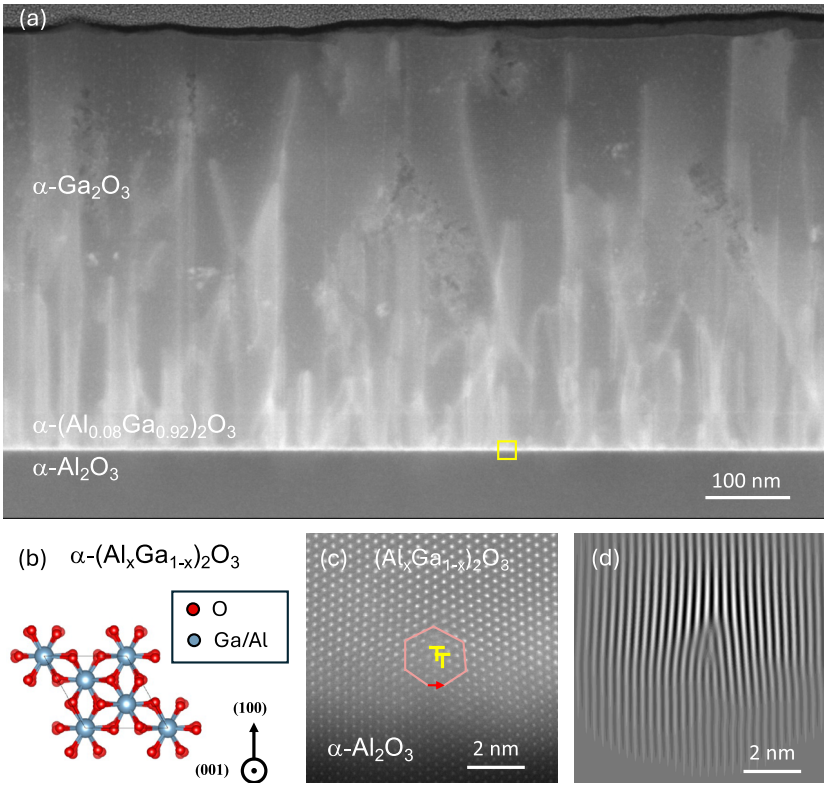

FIG. 7. (a) A LAADF image of film G5 showing the entire film cross-section along the (001) projection showing a density of threading dislocations of (5.6 ± 0.6) × 10^{10} cm^{-2}. The green arrows point to two regions of non-crystalline material. (b) A model of the (001) projection of the α-$(Al_xGa_{1-x})_2O_3$ structure. The red atoms are the oxygen sublattice, and the blue atoms are the octahedrally coordinated aluminum and gallium atoms. (c) An ADF image of the substrate–buffer interface near a pair of dislocations shows that the aluminum and gallium sublattices of the α-$(Al_xGa_{1-x})_2O_3$ buffer remain ordered during relaxation. This region is marked by the yellow square in (a). A Burgers circuit is drawn to highlight the direction of the Burgers vector. (d) A Fourier filtered image that exhibits how the threading dislocation cores are generated by masking the $1\bar{2}10$ fast Fourier transform (FFT) peak of the same region in (c).

screw dislocation densities are estimated by $D_e = \frac{K_{tilt}^2}{2\pi \ln(2) b_e^2}$ and $D_s = \frac{K_{twist}^2}{2\pi \ln(2) b_s^2}$, respectively, where b_e and b_s are the respective magnitudes of the Burgers vectors of the edge and screw dislocations. The density estimates for our film are D_e = 1.1 × 10^{10} cm^{-2} and D_s = 1.7 × 10^{10} cm^{-2}, predicting a total density of threading dislocations of $D \approx 2.8 \times 10^{10}$ cm^{-2}. This density of threading dislocations is around half of typical values reported in the literature for films of similar thicknesses.[33,34] The value is also consistent with the mobility of our films becoming dislocation-limited at a carrier concentration 2.2 × 10^{18} cm^{-3}.[27,31–35]

Film G5 was investigated by low-angle annular dark-field (LAADF-STEM) imaging to assess the density of threading dislocations. Figure 7(a) shows an LAADF image of the film cross-section along the (001) projection. Figure 7(b) is a model of the α-$(Al_xGa_{1-x})_2O_3$ lattice along the same (001) projection for reference. Figure 7(c) shows an ADF image of a diffuse substrate–buffer interface in which a pair of edge dislocations is present along the interface to accommodate the structural relaxation. Figure 7(d) shows a Fourier filtered image that exhibits the threading dislocation cores generated by masking the $1\bar{2}10$ fast Fourier transform (FFT) peak.

The STEM imaging confirms that the threading dislocations originate during the structural relaxation in the buffer layer. This supports the idea that optimizing the buffer to reduce threading dislocation density is key to achieving high-quality α-Ga_2O_3 growth and improving the transport properties in the future. In Fig. 7(a), the threading dislocation density was measured to be (5.6 ± 0.6) × 10^{10} cm^{-2} across the α-Ga_2O_3 film. These threading dislocations are part of dislocation half-loops. The segment of these half loops lying at the interface between the α-Ga_2O_3 and α-Al_2O_3 is a misfit dislocation segment. These segments are needed to relax the lattice mismatch between α-Ga_2O_3 and α-Al_2O_3. Ideally, this network of misfit dislocations would be present at only the interface, with no threading segments. The dislocation density was measured at four locations near the surface of α-Ga_2O_3, middle of α-Ga_2O_3 film, right above the buffer layer, and within the buffer layer. The measured dislocation density at these four locations was constant within the error of the measurement when the increase in thickness of the STEM lamella wedge was taken into consideration. The reported dislocation density assumes a 25 nm thickness of the lamella wedge at the α-Ga_2O_3 surface. This wedge thickness is scaled proportional to the change in intensity from a high-angle annular dark-field (HAADF-STEM) image. This measured density of threading dislocations is relatively low for the film thicknesses compared to other conducting α-Ga_2O_3 films on which STEM has been performed and is within approximately a factor of 2 of the XRD-based estimation shown in Fig. S6 of the supplementary material. This shows that the XRD-based estimation may be a useful tool for estimating the threading dislocation density of α-Ga_2O_3 thin films grown on *m*-plane sapphire in addition to *c*-plane sapphire.[33]

The high density of threading dislocations increases the chance that the silicon donors migrate to a dislocation core and deactivate. At the threading dislocation densities seen in the STEM imaging, Read cylinders formed around the threading dislocations can be expected to cause carrier depletion and prevent mobile donors below a critical mobile n_e of ~1×10^{18} cm^{-3}.[56,57] Compensation by traps from 0D defects, such as chemical impurities, are also expected to further impact carrier depletion.[58] A combination of carrier depletion by dislocations and impurities is consistent with no measurable conductivity being observed in films with $n_e < 4.2 \times 10^{17}$ cm^{-3} due to complete deactivation of the donors.

In Fig. 7(a), dark, splotchy regions of non-crystalline material are also visible where the α-Ga_2O_3 lattice is disrupted. The green arrows point to two examples of these regions. It is unclear at this point what causes these regions to appear and how much they impact the transport properties. Most non-crystalline regions appear near the surface and along dislocation cores, but some regions occasionally appear far from the surface. We suspect that these regions form after growth since there is no impurity phase signal in the optical bandgap measurements with ellipsometry. The ellipsometry measurements occurred before any additional processing was done to the samples, including the HCl surface treatment. Since amorphous Ga_2O_3 has a bandgap of 4.1 eV, we would expect these signals to cause the ellipsometry measurements to read a substantially lower E_g than that of α-Ga_2O_3. As shown in Fig. S7 of the supplementary material, all ellipsometry measurements on these films show bandgaps of 5.36 eV or higher, which suggests that the regions of amorphous Ga_2O_3 form during post-processing of contacts.

In Fig. 7(c), a Burgers circuit is drawn to highlight the direction of the Burgers vector. The Burgers vector represents a single unit cell shift in the [010] direction along the (100) plane, which has dissociated into the two edge dislocations present. The Burgers circuit highlights that the misfit stress is being relieved by the formation of two partial edge dislocations of the ⟨110⟩ type. This relaxation of misfit stress by the dissociation into two partial edge dislocations is observed consistently across the substrate–buffer interface and allows for the aluminum and gallium sublattice to remain ordered. Annealing the buffer layers at elevated T_{sub} may provide enough thermal energy for threading dislocation segments to annihilate with each other, leading to dislocation half loops with longer misfit dislocation segments at the interface and a reduction in the threading dislocation density. The absence of these threading dislocations in the buffer layer should result in a lower threading dislocation being inherited by the conductive overlayer, which is subsequently grown at lower temperatures, and improve the transport properties further.

CONCLUSIONS

Previously, even with record structural quality enabled by *S*-MBE, achieving conductivity in single-layer films remained elusive.[22] We now establish that the implementation of α-Ga_2O_3 and preferably α-$(Al_xGa_{1-x})_2O_3$ as a buffer layer, similar to what has been shown by PLD, provides an effective fix for this issue.[26] This buffer is deposited at a high temperature and acts as a pseudo-substrate that can template α-Ga_2O_3 growth.[26] The addition of aluminum to the buffer to form α-$(Al_xGa_{1-x})_2O_3$ is effective for suppressing any formation of β-Ga_2O_3 and improves the structural quality of the epitaxial Si-doped α-Ga_2O_3 film. By implementing buffer layers, we show that it is possible to grow conductive Si-doped α-Ga_2O_3 at temperatures as low as 425 °C, reaffirming that α-Ga_2O_3 is the widest bandgap semiconductor with BEOL-compatible growth conditions. Our results show that $T_{sub} \leq 500$ °C and $P_{O3} \geq 1 \times 10^{-6}$ Torr are necessary for the highly reproducible growth of conductive Si-doped α-Ga_2O_3 thin films by *S*-MBE. SIMS measurements confirm that silicon is incorporated in the α-Ga_2O_3 thin films both inside and outside of this ideal range of growth conditions but is only electrically active inside the ideal range. The lack of conductivity in films grown at elevated T_{sub} is believed to be a result of silicon incorporating as Si^{2+} or diffusing to the threading dislocations and forming Cottrell atmospheres.[26,53–55]

Under these optimized growth conditions, mobilities as high as 90 $\frac{cm^2}{V \cdot s}$ and conductivities as high as 646 S/cm at room temperature were achieved. Both are the highest values for α-Ga_2O_3 thin films grown by any method to date. Compared to α-Ga_2O_3 thin films grown by PLD, HVPE, and mist CVD, our *S*-MBE grown films have higher mobilities for carrier concentrations of $n \geq 2.2 \times 10^{18}$ cm^{-3}, and the highest mobilities ever demonstrated at any *n*. The rocking curves of our Si-doped α-Ga_2O_3 thin films also have FWHM that are nearly 20% narrower than the narrowest values reported for Si-doped α-Ga_2O_3 on *m*-plane sapphire.

Cross-sectional STEM on one α-Ga_2O_3 film shows that $(5.6 \pm 0.6) \times 10^{10}$ cm^{-2} threading dislocations were generated during the structural relaxation of the buffer layer and reach the surface of the Si-doped α-Ga_2O_3 overlayer. We also confirm that a combination of symmetric and asymmetric rocking curves can give a reasonable estimate (within approximately a factor of two) for the dislocation density in α-Ga_2O_3 thin films grown on *m*-plane sapphire. The density of threading dislocations is relatively low for the film thicknesses of conducting α-Ga_2O_3 films but is unlikely to fully explain the improved transport properties. We instead suspect that high activation ratios and improved chemical purity available with *S*-MBE growth are the primary reasons for the higher mobilities in our films.

The main challenge to further improve transport behavior in α-Ga_2O_3 thin films, especially for $N_D \leq 10^{18}$ cm^{-3}, is finding a way to reduce the threading dislocation densities in the doped α-Ga_2O_3 film. This is significant because it could allow α-Ga_2O_3 to achieve a BFOM multiple times the maximum possible for doped β-Ga_2O_3. We believe that optimizing the growth conditions of the α-$(Al_xGa_{1-x})_2O_3$ buffer layer is the key to reducing dislocation densities in α-$(Al_xGa_{1-x})_2O_3$ films and maximizing transport properties. The simplest method is growing thicker buffer layers in the same conditions to give the threading dislocations a greater opportunity to terminate with one another. A second option is the use of compositionally graded α-$(Al_xGa_{1-x})_2O_3$ buffer layers. Another option, which we see as most favorable, is altering the growth conditions of the buffer layers by *in situ* annealing the buffers to lower their threading dislocation densities and create superior α-$(Al_xGa_{1-x})_2O_3$ pseudosubstrates.

SUPPLEMENTARY MATERIALS

See the supplementary material for additional figures and data about the substrates, α-$(Al_xGa_{1-x})_2O_3$ buffer layers, Ti/Au contacts, and Si-doped α-Ga_2O_3 layers.

ACKNOWLEDGMENTS

This work was primarily supported by the AFOSR/AFRL ACCESS Center of Excellence under Award No. FA9550-18-1-0529. This work was supported in part by SUPREME, one of seven centers supported by the Semiconductor Research Corporation (SRC) and DARPA under the Joint University Microelectronics Program 2.0 (JUMP 2.0). This work made use of the Cornell Energy Systems Institute Shared Facilities, partly sponsored by the NSF (Grant No. MRI DMR-1631282). The STEM work also made use of the electron microscopy facility of the Cornell Center for Materials Research (CCMR) with support from the National Science Foundation Materials Research Science and Engineering Centers (MRSEC) program (Grant No. DMR-1719875). N.A.P. acknowledges support from the National Science Foundation Graduate Research Fellowship under Grant No. DGE2139899. The Thermo Fisher Spectra 300 X-CFEG was acquired with support from PARADIM, an NSF MIP (Grant No. DMR-2039380), and Cornell University. M.K.I.S., M.D.W., and D.G.S. acknowledge additional funding from Grant No. NSF-PREM-DMR-2122147.

We lastly personally thank Steven Button for preparing all the substrates used in these experiments as well as designing the shadow mask for Ti/Au contact deposition. We would also like to thank Cameron Gorsak for his advice on the experiments and for making the sapphire shadow masks for the highly Si-doped regrown contacts.

AUTHOR DECLARATIONS

Conflict of Interest

The author D.G.S. has been granted U.S. Patent No. 11,462,402 (4 October 2022) with the title "Suboxide Molecular-Beam Epitaxy and Related Structures."

Author Contributions

Jacob Steele: Conceptualization (equal); Data curation (lead); Formal analysis (lead); Investigation (lead); Methodology (lead); Project administration (supporting); Supervision (supporting); Validation (supporting); Visualization (lead); Writing – original draft (lead); Writing – review & editing (supporting). **Julianne Chen**: Data curation (equal); Formal analysis (supporting); Investigation (supporting); Methodology (supporting); Visualization (supporting); Writing – review & editing (supporting). **Tamá Burrell**: Data curation (supporting); Investigation (supporting); Visualization (supporting). **Naomi A. Pieczulewski**: Data curation (supporting); Formal analysis (supporting); Investigation (supporting); Visualization (supporting); Writing – original draft (supporting); Writing – review & editing (supporting). **Debaditya Bhattacharya**: Data curation (supporting); Formal analysis (supporting); Investigation (supporting); Writing – original draft (supporting). **Kathleen Smith**: Data curation (supporting); Formal analysis (supporting); Investigation (supporting). **Katie Gann**: Formal analysis (supporting); Methodology (supporting); Supervision (supporting). **Michael O. Thompson**: Conceptualization (supporting); Formal analysis (supporting); Funding acquisition (supporting); Project administration (supporting); Resources (supporting); Supervision (supporting). **Huili G. Xing**: Conceptualization (supporting); Funding acquisition (supporting); Project administration (supporting); Resources (supporting); Software (supporting); Supervision (supporting); Validation (supporting); Writing – review & editing (supporting). **Debdeep Jena**: Conceptualization (supporting); Funding acquisition (supporting); Methodology (supporting); Project administration (supporting); Resources (supporting); Software (supporting); Supervision (supporting); Validation (supporting); Writing – review & editing (supporting). **David A. Muller**: Formal analysis (supporting); Funding acquisition (supporting); Methodology (supporting); Project administration (supporting); Resources (supporting); Software (supporting); Supervision (supporting); Validation (supporting); Visualization (supporting). **Michael D. Williams**: Data curation (supporting); Formal analysis (supporting); Funding acquisition (supporting); Investigation (supporting); Methodology (supporting); Project administration (supporting); Resources (supporting); Software (supporting); Validation (supporting); Visualization (supporting); Writing – review & editing (supporting). **M.K. Indika Senevirathna**: Data curation (supporting); Formal analysis (supporting); Funding acquisition (supporting); Investigation (supporting); Methodology (supporting); Project administration (supporting); Resources (supporting); Software (supporting); Supervision (supporting); Validation (supporting); Visualization (supporting); Writing – review & editing (supporting). **Darrell. G. Schlom**: Conceptualization (equal); Formal analysis (equal); Funding acquisition (equal); Methodology (equal); Project administration (equal); Resources (equal); Software (equal); Supervision (equal); Validation (equal); Visualization (equal); Writing – original draft (equal); Writing – review & editing (equal).

DATA AVAILABILITY

The data that support the findings of this study are available within the article and its supplementary material.

REFERENCES

[1] B. J. Baliga, *Fundamentals of Power Semiconductor Devices*, 2nd ed. (Springer, 2019), pp. 14–16.

[2] O. Slobodyan, J. Flicker, J. Dickerson, J. Shoemaker, A. Binder, T. Smith, S. Goodnick, R. Kaplar, and M. Hollis, "Analysis of the dependence of critical electric field on semiconductor bandgap," J. Mater. Res. **37**(4), 849–865 (2022).

[3] Y. Sun, X. Kang, Y. Zheng, J. Lu, X. Tian, K. Wei, H. Wu, W. Wang, X. Liu, and G. Zhang, "Review of the recent progress on GaN-based vertical power Schottky barrier diodes (SBDs)," Electronics **8**(5), 575 (2019).

[4] S. J. Pearton, J. Yang, P. H. Cary, F. Ren, J. Kim, M. J. Tadjer, and M. A. Mastro, "A review of Ga_2O_3 materials, processing, and devices," Appl. Phys. Rev. **5**(1), 011301 (2018).

[5] C. Peterson, A. Bhattacharyya, K. Chanchaiworawit, R. Kahler, S. Roy, Y. Liu, S. Rebollo, A. Kallistova, T. E. Mates, and S. Krishnamoorthy, "200 cm^2 vs electron mobility and controlled low 10^{15} cm^{-3} Si doping in (010) β-Ga_2O_3 epitaxial drift layers," Appl. Phys. Lett. **125**(18), 182103 (2024).

[6]A. Sharma and U. Singisetti, "Low field electron transport in α-Ga_2O_3: An *ab initio* approach," Appl. Phys. Lett. **118**(3), 032101 (2021).
[7]R. Jinno, C. S. Chang, T. Onuma, Y. Cho, S.-T. Ho, D. Rowe, M. C. Cao, K. Lee, V. Protasenko, D. G. Schlom, D. A. Muller, H. G. Xing, and D. Jena, "Crystal orientation dictated epitaxy of ultrawide-bandgap 5.4- to 8.6 eV α-$(AlGa)_2O_3$ on *m*-plane sapphire," Sci. Adv. **7**(2), eabd5891 (2021).
[8]H. He, R. Orlando, M. A. Blanco, R. Pandey, E. Amzallag, I. Baraille, and M. Rérat, "First-principles study of the structural, electronic, and optical properties of Ga_2O_3 in its monoclinic and hexagonal phases," Phys. Rev. B **74**(19), 195123 (2006).
[9]F. Wang, J. Shan, E. Knoesel, M. Bonn, and T. F. Heinz, in *Electronic Charge Transport in Sapphire Studied by optical-pump/THz-probe Spectroscopy*, edited by K.-T. Tsen, J.-J. Song, and H. Jiang (San Jose, CA, 2004), p. 216.
[10]N. Ma, N. Tanen, A. Verma, Z. Guo, T. Luo, H. G. Xing, and D. Jena, "Intrinsic electron mobility limits in β-Ga_2O_3," Appl. Phys. Lett. **109**(21), 212101 (2016).
[11]A. K. Rajapitamahuni, A. K. Manjeshwar, A. Kumar, A. Datta, P. Ranga, L. R. Thoutam, S. Krishnamoorthy, U. Singisetti, and B. Jalan, "Plasmon–phonon coupling in electrostatically gated β-Ga_2O_3 films with mobility exceeding 200 $cm^2\ V^{-1}\ s^{-1}$," ACS Nano **16**(6), 8812–8819 (2022).
[12]D. Yang, B. Kim, T. H. Eom, Y. Park, and H. W. Jang, "Epitaxial growth of Alpha gallium oxide thin films on sapphire substrates for electronic and optoelectronic devices: Progress and perspective," Electron. Mater. Lett. **18**(2), 113–128 (2022).
[13]E. M. Garrity, C.-W. Lee, P. Gorai, M. B. Tellekamp, A. Zakutayev, and V. Stevanović, "Computational identification of ternary wide-band-gap oxides for high-power electronics," PRX Energy **1**(3), 033006 (2022).
[14]H. Son and D.-W. Jeon, "Optimization of the growth temperature of α-Ga_2O_3 epilayers grown by halide vapor phase epitaxy," J. Alloys Compd. **773**, 631–635 (2019).
[15]H. Son, Y. Choi, J.-H. Park, B. Ryu, and D.-W. Jeon, "Correlation of pulsed gas flow on Si-doped α-Ga_2O_3 epilayer grown by halide vapor phase epitaxy," ECS J. Solid State Sci. Technol. **9**(5), 055005 (2020).
[16]M. Lee, M. Yang, H.-Y. Lee, H. U. Lee, H. Lee, H. Son, and U. J. Kim, "The growth of HVPE α-Ga_2O_3 crystals and its solar-blind UV photodetector applications," Mater. Sci. Semicond. Process. **123**, 105565 (2021).
[17]K. Akaiwa, K. Kaneko, K. Ichino, and S. Fujita, "Conductivity control of Sn-doped α-Ga_2O_3 thin films grown on sapphire substrates," Jpn. J. Appl. Phys. **55**(12), 1202BA (2016).
[18]T. Uchida, K. Kaneko, and S. Fujita, "Electrical characterization of Si-doped n-type α-Ga_2O_3 on sapphire substrates," MRS Adv. **3**(3), 171–177 (2018).
[19]G. T. Dang, T. Yasuoka, Y. Tagashira, T. Tadokoro, W. Theiss, and T. Kawaharamura, "Bandgap engineering of α-$(Al_xGa_{1-x})_2O_3$ by a mist chemical vapor deposition two-chamber system and verification of Vegard's law," Appl. Phys. Lett. **113**(6), 062102 (2018).
[20]A. Y. Polyakov, V. I. Nikolaev, S. I. Stepanov, A. I. Pechnikov, E. B. Yakimov, N. B. Smirnov, I. V. Shchemerov, A. A. Vasilev, A. I. Kochkova, A. V. Chernykh, and S. J. Pearton, "Editors' choice—Electrical properties and deep traps in α-Ga_2O_3 Sn films grown on sapphire by halide vapor phase epitaxy," ECS J. Solid State Sci. Technol. **9**(4), 045003 (2020).
[21]R. Kumaran, T. Tiedje, S. E. Webster, S. Penson, and W. Li, "Epitaxial Nd-doped α-$(Al_xGa_{1-x})_2O_3$ films on sapphire for solid-state waveguide lasers," Opt. Lett. **35**(22), 3793 (2010).
[22]J. Steele, K. Azizie, N. Pieczulewski, Y. Kim, S. Mou, T. J. Asel, A. T. Neal, D. Jena, H. G. Xing, D. A. Muller, T. Onuma, and D. G. Schlom, "Epitaxial growth of α-$(Al_xGa_{1-x})_2O_3$ by suboxide molecular-beam epitaxy at 1 μm/h," APL Mater. **12**(4), 041113 (2024).
[23]F. Egyenes-Pörsök, F. Gucmann, K. Hušeková, E. Dobročka, M. Sobota, M. Mikolášek, K. Fröhlich, and M. Ťapajna, "Growth of α- and β-Ga_2O_3 epitaxial layers on sapphire substrates using liquid-injection MOCVD," Semicond. Sci. Technol. **35**(11), 115002 (2020).
[24]H. Okumura and J. B. Varley, "MOCVD growth of Si-doped α-$(AlGa)_2O_3$ on *m*-plane α-Al_2O_3 substrates," Jpn. J. Appl. Phys. **63**(7), 075502 (2024).
[25]M. Kneiß, D. Splith, H. Von Wenckstern, M. Lorenz, T. Schultz, N. Koch, and M. Grundmann, "Strain states and relaxation for α-$(Al_xGa_{1-x})_2O_3$ thin films on prismatic planes of α-Al_2O_3 in the full composition range: Fundamental difference of a- and m-epitaxial planes in the manifestation of shear strain and lattice tilt," J. Mater. Res. **36**(23), 4816–4831 (2021).
[26]S. Vogt, C. Petersen, M. Kneiß, D. Splith, T. Schultz, H. Von Wenckstern, N. Koch, and M. Grundmann, "Realization of conductive n-type doped α-Ga_2O_3 on *m*-plane sapphire grown by a two-step pulsed laser deposition process," Phys. Status Solidi A **220**(3), 2200721 (2023).
[27]J. P. McCandless, D. Rowe, N. Pieczulewski, V. Protasenko, M. Alonso-Orts, M. S. Williams, M. Eickhoff, H. G. Xing, D. A. Muller, D. Jena, and P. Vogt, "Growth of α-Ga_2O_3 on α-Al_2O_3 by conventional molecular-beam epitaxy and metal–oxide-catalyzed epitaxy," Jpn. J. Appl. Phys. **62**(SF), SF1013 (2023).
[28]H. Okumura, A. Fassion, and C. Mannequin, "Si-doped $(AlGa)_2O_3$ growth on a-m- and r-plane α-Al_2O_3 substrates by molecular beam epitaxy," Jpn. J. Appl. Phys. **63**(5), 055502 (2024).
[29]J. P. McCandless, C. S. Chang, K. Nomoto, J. Casamento, V. Protasenko, P. Vogt, D. Rowe, K. Gann, S. T. Ho, W. Li, R. Jinno, Y. Cho, A. J. Green, K. D. Chabak, D. G. Schlom, M. O. Thompson, D. A. Muller, H. G. Xing, and D. Jena, "Thermal stability of epitaxial α-Ga_2O_3 and $(Al,Ga)_2O_3$ layers on m-plane sapphire," Appl. Phys. Lett. **119**(6), 062102 (2021).
[30]K. Akaiwa, K. Ota, T. Sekiyama, T. Abe, T. Shinohe, and K. Ichino, "Electrical properties of Sn-doped α-Ga_2O_3 films on m-plane sapphire substrates grown by mist chemical vapor deposition," Phys. Status Solidi A **217**(3), 1900632 (2020).
[31]D. Wickramaratne, J. B. Varley, and J. L. Lyons, "Donor doping of corundum $(Al_xGa_{1-x})_2O_3$," Appl. Phys. Lett. **121**(4), 042110 (2022).
[32]K. Kaneko, H. Kawanowa, H. Ito, and S. Fujita, "Evaluation of misfit relaxation in α-Ga_2O_3 epitaxial growth on α-Al_2O_3 substrate," Jpn. J. Appl. Phys. **51**(2R), 020201 (2012).
[33]T. C. Ma, X. H. Chen, Y. Kuang, L. Li, J. Li, F. Kremer, F.-F. Ren, S. L. Gu, R. Zhang, Y. D. Zheng, H. H. Tan, C. Jagadish, and J. D. Ye, "On the origin of dislocation generation and annihilation in α-Ga_2O_3 epilayers on sapphire," Appl. Phys. Lett. **115**(18), 182101 (2019).
[34]H. Takane, S. Konishi, Y. Hayasaka, R. Ota, T. Wakamatsu, Y. Isobe, K. Kaneko, and K. Tanaka, "Structural characterization of threading dislocation in α-Ga_2O_3 thin films on *c*- and *m*-plane sapphire substrates," J. Appl. Phys. **136**(2), 025105 (2024).
[35]H. Takane, H. Izumi, H. Hojo, T. Wakamatsu, K. Tanaka, and K. Kaneko, "Effect of dislocations and impurities on carrier transport in α-Ga_2O_2 on *m*-plane sapphire substrate," J. Mater. Res. **38**(10), 2645–2654 (2023).
[36]P. Vogt, F. V. E. Hensling, K. Azizie, C. S. Chang, D. Turner, J. Park, J. P. McCandless, H. Paik, B. J. Bocklund, G. Hoffman, O. Bierwagen, D. Jena, H. G. Xing, S. Mou, D. A. Muller, S.-L. Shang, Z.-K. Liu, and D. G. Schlom, "Adsorption-controlled growth of Ga_2O_3 by suboxide molecular-beam epitaxy," APL Mater. **9**(3), 031101 (2021).
[37]K. Azizie, F. V. E. Hensling, C. A. Gorsak, Y. Kim, N. A. Pieczulewski, D. M. Dryden, M. K. I. Senevirathna, S. Coye, S.-L. Shang, J. Steele, P. Vogt, N. A. Parker, Y. A. Birkhölzer, J. P. McCandless, D. Jena, H. G. Xing, Z.-K. Liu, M. D. Williams, A. J. Green, K. Chabak, D. A. Muller, A. T. Neal, S. Mou, M. O. Thompson, H. P. Nair, and D. G. Schlom, "Silicon-doped β-Ga_2O_3 films grown at 1 μm/h by suboxide molecular-beam epitaxy," APL Mater. **11**(4), 041102 (2023).
[38]H.-J. Lee, K. Fujii, T. Goto, T. Yao, and J. Chang, "Effects of controlled ambidirectional nucleation on the heteroepitaxial growth of *m*-GaN on *m*-Sapphire," Appl. Phys. Lett. **98**(7), 071904 (2011).
[39]T. J. Smart, F. V. E. Hensling, D. Y. Kim, L. N. Majer, Y. E. Suyolcu, D. Dereh, D. G. Schlom, D. Jena, J. Mannhart, and W. Braun, "Why thermal laser epitaxy aluminum sources yield reproducible fluxes in oxidizing environments," J. Vac. Sci. Technol. A **41**(4), 042701 (2023).
[40]S.-L. Shang, S. Lin, M. C. Gao, D. G. Schlom, and Z.-K. Liu, "Ellingham diagrams of binary oxides," APL Mater. **12**(8), 081110 (2024).
[41]K. M. Adkison, S.-L. Shang, B. J. Bocklund, D. Klimm, D. G. Schlom, and Z.-K. Liu, "Suitability of binary oxides for molecular-beam epitaxy source materials: A comprehensive thermodynamic analysis," APL Mater. **8**(8), 081110 (2020).
[42]F. Massabuau, D. Nicol, F. Adams, J. Jarman, J. Roberts, A. Kovács, P. Chalker, and R. Oliver, "Study of Ti contacts to corundum α-Ga_2O_3," J. Phys. D: Appl. Phys. **54**(38), 384001 (2021).
[43]M. Hilfiker, R. Korlacki, R. Jinno, Y. Cho, H. G. Xing, D. Jena, U. Kilic, M. Stokey, and M. Schubert, "Anisotropic dielectric functions, band-to-band transitions, and critical points in α-Ga_2O_3," Appl. Phys. Lett. **118**(6), 062103 (2021).

[44]E. H. Smith, P. D. C. King, A. Soukiassian, D. G. Ast, and D. G. Schlom, "Hybrid reflections from multiple x-ray scattering in epitaxial oxide films," Appl. Phys. Lett. **111**(13), 131903 (2017).
[45]T. Kawaharamura, G. T. Dang, and M. Furuta, "Successful growth of conductive highly crystalline Sn-doped α-Ga_2O_3 thin films by fine-channel mist chemical vapor deposition," Jpn. J. Appl. Phys. **51**(4R), 040207 (2012).
[46]V. D. Wheeler, N. Nepal, D. R. Boris, S. B. Qadri, L. O. Nyakiti, A. Lang, A. Koehler, G. Foster, S. G. Walton, C. R. Eddy, and D. J. Meyer, "Phase control of crystalline Ga_2O_3 films by plasma-enhanced atomic layer deposition," Chem. Mater. **32**(3), 1140–1152 (2020).
[47]K. Ikenaga, N. Tanaka, T. Nishimura, H. Iino, K. Goto, M. Ishikawa, H. Machida, T. Ueno, and Y. Kumagai, "Effect of high temperature homoepitaxial growth of β-Ga_2O_3 by hot-wall metalorganic vapor phase epitaxy," J. Cryst. Growth **582**, 126520 (2022).
[48]C. W. Magee, "Depth profiling of trace constituents using secondary ion mass-spectrometry," J. Res. Natl. Bur. Stand. **93**(3), 390 (1988).
[49]A. Budrevich and J. Hunter, "Metrology aspects of SIMS depth profiling for advanced ULSI processes," in *1998 International Conference on Characterization and Metrology for ULSI Technology* (ASCE, Gaithersburg, MD, 1998), pp. 169–181.
[50]W. T. Read, "XVI. Scattering of electrons by charged dislocations in semiconductors," London, Edinburgh Dublin Philos. Mag. J. Sci. **46**(373), 111–131 (1955).
[51]W. T. Read, "LXXXVII. Theory of dislocations in germanium," London, Edinburgh Dublin Philos. Mag. J. Sci. **45**(367), 775–796 (1954).
[52]A. H. Cottrell and B. A. Bilby, "Dislocation theory of yielding and strain ageing of iron," Proc. Phys. Soc., Sect. A **62**(1), 49–62 (1949).
[53]K. Thompson, P. L. Flaitz, P. Ronsheim, D. J. Larson, and T. F. Kelly, "Imaging of arsenic Cottrell atmospheres around silicon defects by three-dimensional atom probe tomography," Science **317**(5843), 1370–1374 (2007).
[54]S. Duguay, T. Philippe, F. Cristiano, and D. Blavette, "Direct imaging of boron segregation to extended defects in silicon," Appl. Phys. Lett. **97**(24), 242104 (2010).
[55]S. Duguay, A. Echeverri, C. Castro, and O. Latry, "Evidence of Mg segregation to threading dislocation in normally-off GaN-HEMT," IEEE Trans. Nanotechnol. **18**, 995–998 (2019).
[56]T. Yokoyama, R. Takenaka, Y. Kamimura, K. Edagawa, and I. Yonenaga, "Direct observation of carrier depletion around a dislocation in GaP by scanning spreading resistance microscopy," Appl. Phys. Lett. **95**(20), 202108 (2009).
[57]E. Baghani and S. K. O'Leary, "Threading dislocation lines within indium nitride versus gallium nitride: The implications of different dominant dislocation line charge screening mechanisms," Solid State Commun. **352**, 114833 (2022).
[58]M. Labed, N. Sengouga, C. Venkata Prasad, M. Henini, and Y. S. Rim, "On the Nature of majority and minority traps in β-Ga_2O_3: A review," Mater. Today Phys. **36**, 101155 (2023).

APL Materials

ERRATUM | DECEMBER 01 2025

Erratum: “Growth of conductive Si-doped α-Ga_2O_3 by suboxide molecular-beam epitaxy” [APL Mater. 13, 101117 (2025)] FREE

Jacob Steele ; Julianne Chen ; Tamá Burrell; Naomi A. Pieczulewski ; Debaditya Bhattacharya ; Kathleen Smith ; Katie Gann ; Michael O. Thompson ; Huili G. Xing ; Debdeep Jena ; David A. Muller ; Michael D. Williams ; M. K. Indika Senevirathna ; Darrell G. Schlom

APL Mater. 13, 129901 (2025)
https://doi.org/10.1063/5.0309396

AIP Publishing

Erratum: "Growth of conductive Si-doped α-Ga_2O_3 by suboxide molecular-beam epitaxy" [APL Mater. 13, 101117 (2025)]

Cite as: APL Mater. 13, 129901 (2025); doi: 10.1063/5.0309396
Submitted: 27 October 2025 • Accepted: 8 November 2025 •
Published Online: 1 December 2025

Jacob Steele,[1] Julianne Chen,[2] Tamá Burrell,[3] Naomi A. Pieczulewski,[1] Debaditya Bhattacharya,[4] Kathleen Smith,[4] Katie Gann,[1] Michael O. Thompson,[1] Huili G. Xing,[1,4,5] Debdeep Jena,[1,4,5] David A. Muller,[5,6] Michael D. Williams,[3] M. K. Indika Senevirathna,[3] and Darrell G. Schlom[1,5,7,a)]

AFFILIATIONS

[1] Department of Materials Science and Engineering, Cornell University, Ithaca, New York 14853, USA
[2] Platform for the Accelerated Realization, Analysis, and Discovery of Interface Materials (PARADIM), Cornell University, Ithaca, New York 14853, USA
[3] Department of Physics, Clark Atlanta University, Atlanta, Georgia 30314, USA
[4] School of Electrical and Computer Engineering, Cornell University, Ithaca, New York 14853, USA
[5] Kavli Institute at Cornell for Nanoscale Science, Ithaca, New York 14853, USA
[6] School of Applied and Engineering Physics, Cornell University, Ithaca, New York 14853, USA
[7] Leibniz-Institut für Kristallzüchtung, Max-Born-Str. 2, 12489 Berlin, Germany

[a)] **Author to whom correspondence should be addressed:** schlom@cornell.edu

https://doi.org/10.1063/5.0309396

In our recently published paper,[1] a reference was mistakenly cited as support for our hypothesis on p. 9 that Si^{4+} may be converting to Si^{2+} and acting as a compensating defect in α-Ga_2O_3. The source does not support our hypothesis as its claim is that Sn^{4+} converting to Sn^{2+} may be a compensating defect in α-Ga_2O_3.[2]

Without the supporting reference, we withdraw the hypothesis and the section of text should read as follows: "One hypothesis that could explain this behavior is that at elevated T_{sub}, the silicon dopant has a longer diffusion length and enough thermal energy to diffuse to and get pinned at a dislocation, where it forms a Cottrell atmosphere." This is opposed to how the text appears in the published version: "Several hypotheses could explain this behavior. One is that when incorporated at elevated T_{sub}, significant concentrations of Si incorporate in the 2+ oxidation state and act as compensating defects.[26] Another is that at elevated T_{sub}, the silicon dopant has a longer diffusion length and enough thermal energy to diffuse to and get pinned at a dislocation, where it forms a Cottrell atmosphere.[52]"

REFERENCES

[1] J. Steele, J. Chen, T. Burrell, N. A. Pieczulewski, D. Bhattacharya, K. Smith, K. Gann, M. O. Thompson, H. G. Xing, D. Jena, D. A. Muller, M. D. Williams, M. K. I. Senevirathna, and D. G. Schlom, "Growth of conductive Si-doped α-Ga_2O_3 by suboxide molecular-beam epitaxy," APL Mater. **13**(10), 101117 (2025).
[2] S. Vogt, C. Petersen, M. Kneiß, D. Splith, T. Schultz, H. Von Wenckstern, N. Koch, and M. Grundmann, "Realization of conductive n-type doped α-Ga_2O_3 on m-plane sapphire grown by a two-step pulsed laser deposition process," Phys. Status Solidi A **220**(3), 2200721 (2023).

Supplementary Material for "Epitaxial Growth of Conductive Si-Doped α-Ga_2O_3 by Suboxide Molecular-Beam Epitaxy"

Jacob Steele,[1] Julianne Chen,[2] Tamá Burrell,[3] Naomi A. Pieczulewski,[1] Debaditya Bhattacharya,[4] Kathleen Smith,[4] Katie Gann,[1] Michael O. Thompson,[1] David A. Muller,[5,6] Huili G. Xing,[1,4,5] Debdeep Jena,[1,4,5] Michael D. Williams,[3] M.K. Indika Senevirathna,[3] and Darrell. G. Schlom[1,5,7]

[1)] Department of Materials Science and Engineering, Cornell University, Ithaca, New York 14853, USA

[2)] Platform for the Accelerated Realization, Analysis, and Discovery of Interface Materials (PARADIM), Cornell University, Ithaca, New York 14853, USA

[3)] Department of Physics, Clark Atlanta University, Atlanta, Georgia, 30314, USA

[4)] School of Electrical and Computer Engineering, Cornell University, Ithaca, New York 14853, USA

[5)] Kavli Institute at Cornell for Nanoscale Science, Ithaca, New York 14853, USA

[6)] School of Applied and Engineering Physics, Cornell University, Ithaca, New York, 14853, USA

[7)] Leibniz-Institut für Kristallzüchtung, Max-Born-Str. 2, 12489 Berlin, Germany

(Dated: 28 August 2025)

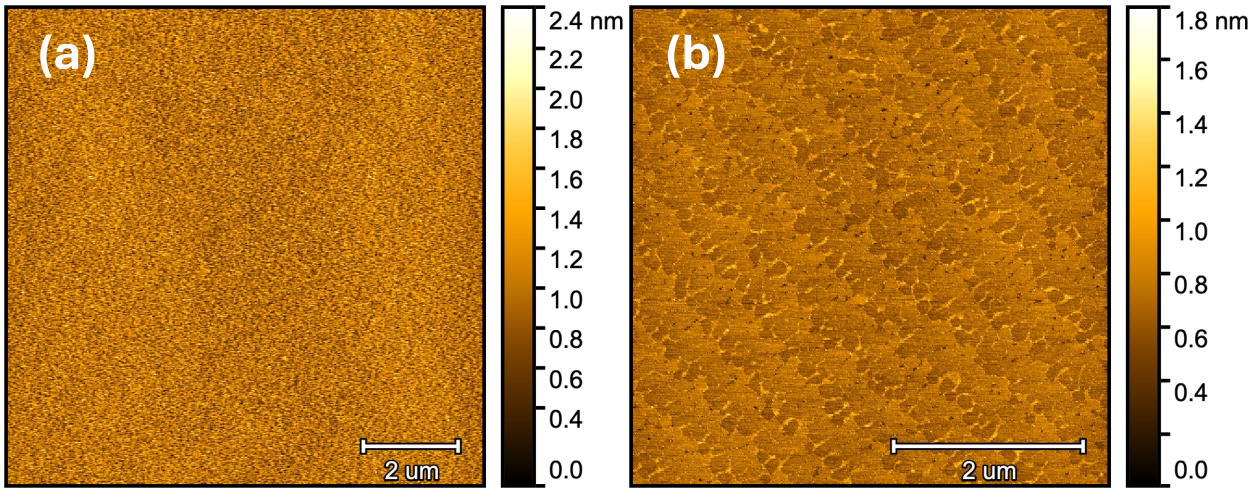

Fig. S1. Atomic force microscopy (AFM) images of two *m*-plane α-Al_2O_3 substrates after annealing in air at 1000 °C for 5 h. **(a)** A 10 µm × 10 µm image of a typical "flat" substrate, where there are no step edges or other features visible. The surface is virtually identical to the as-received state. The substrate has an rms roughness of 0.26 nm. **(b)** A 5 µm × 5 µm image of a typical "stepped" substrate, where there are steps with rough step edges visible. The substrate has an rms roughness of 0.12 nm.

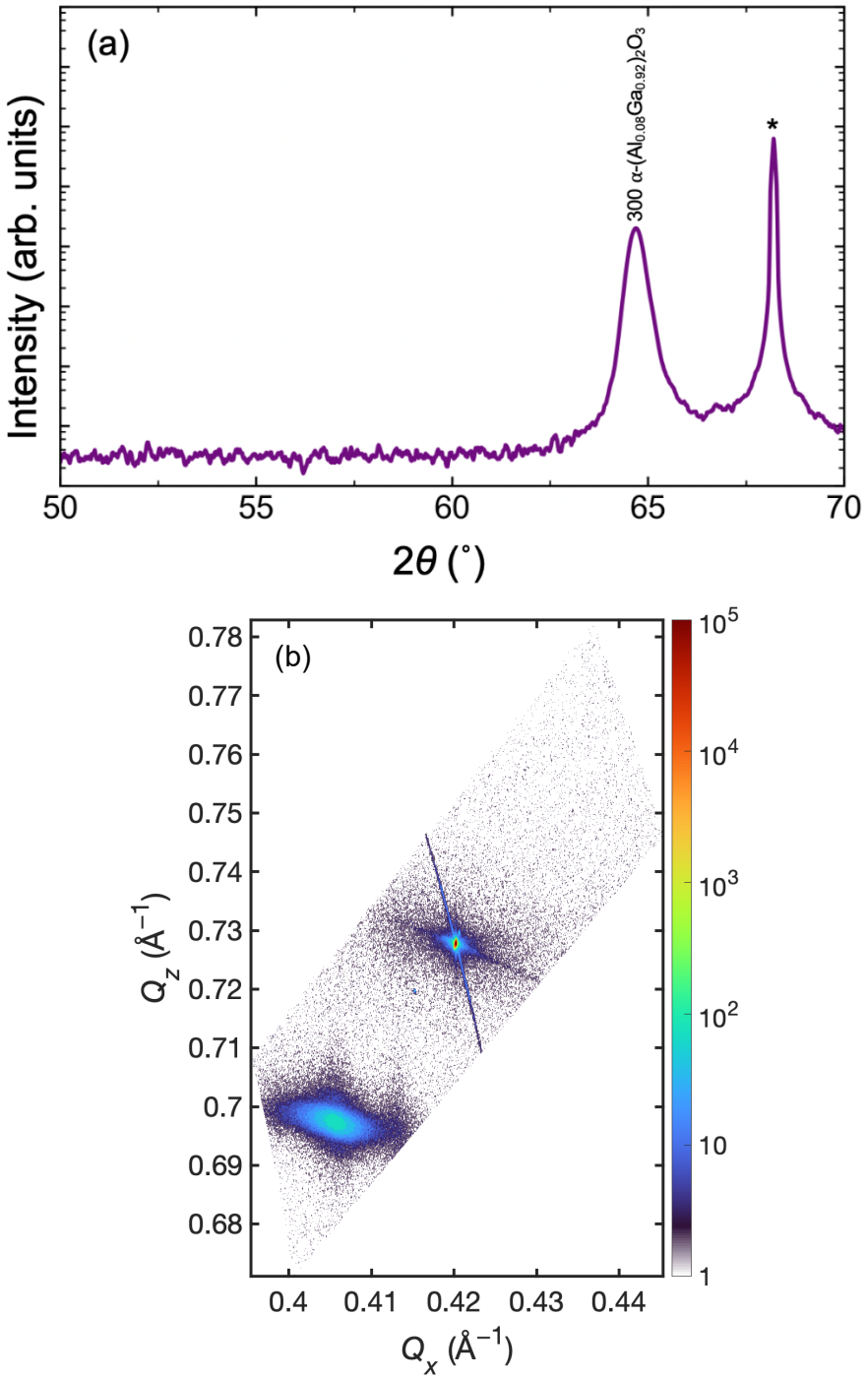

Fig. S2. (a) A θ-2θ plot over the range of $2\theta = 50°$ - $70°$ of a 38 nm thick α-$(Al_{0.08}Ga_{0.92})_2O_3$ buffer layer that was grown for 10 min at at $P_{80\%\ O_3} = 5 \times 10^{-6}$ Torr and $T_{sub} = 750$ ˚C. The 300 peak of the α-Al_2O_3 substrate is marked by the * and the 300 α-$(Al_{0.08}Ga_{0.92})_2O_3$ peak is labeled. **(b)** An RSM of the 220 reflections of the film and substrate. The substrate peak is the narrow, intense peak at the center of the image and the film peak is the broad, weaker peak near $Q_x = 0.405$ Å^{-1} and $Q_z = 0.697$ Å^{-1}.

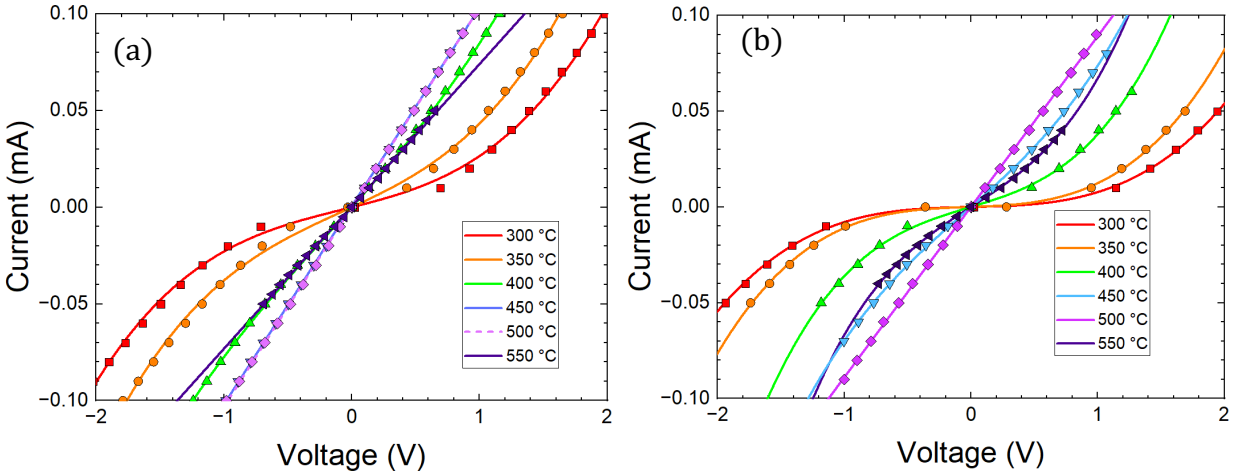

FIG S3. (a) A plot of superimposed current-voltage measurements between two contacts on sample G27 after annealing for 2 minutes in flowing N_2 at 300 °C – 550 °C in 50 °C steps. The color of the lines and data points reflect the temperature of the anneal conducted just before the measurement. The data points are the measured values, and the lines are a third-order polynomial fit to these data points. **(b)** A plot of superimposed *I-V* measurements between two separate contacts on sample G27 after annealing at 300 °C – 550 °C in 50 °C steps.

To determine which annealing conditions produce the most ideal behavior in Ti/Au contacts to α-Ga_2O_3, we performed an annealing series on sample G27. Two *I-V* curves were measured after each anneal, each between an adjacent set of van der Pauw corner contacts 1 - 2 and 3 - 4. Each anneal step was for 2 minutes in a flowing N_2 ambient. Figure S3 shows the resulting *I-V* curves after each anneal. Figure S3 (a) shows the measurements between contacts 1 and 2 and Fig. S3 (b) shows the measurements between contacts 3 and 4. After the Ti/Au deposition, both sets of contacts showed Schottky-type behavior with high contact resistance. After the first anneal at 300 °C, the contacts continued to show Schottky-type behavior with little reduction in the contact resistance. The behavior of all contacts became increasingly ohmic with each annealing step until the 500 °C anneal. Contacts 1 and 2 showed nearly linear ohmic behavior after the 400 °C anneal and remained so even after the highest 550 °C anneal step. Both the 450 °C and 500 °C anneals led to the most ideal behavior for contacts 1 and 2, with very little

difference in behavior between the two annealing temperatures. Contacts 3 and 4 displayed nearly linear-ohmic behavior only after the 450 °C and 500 °C anneals, with the most ideal behavior occurring after the 500 °C anneal. Both sets of contacts showed degradation with higher resistance after the 550 °C anneal, signaling over-annealing. As the 500 °C anneal led to both sets of contacts showing nearly linear ohmic behavior with minimal resistance, we selected 500 °C for 2 min in an N_2 atmosphere as our annealing recipe for Ti/Au contacts to α-Ga_2O_3. All other samples in this paper use this recipe for the Ti/Au post-anneal.

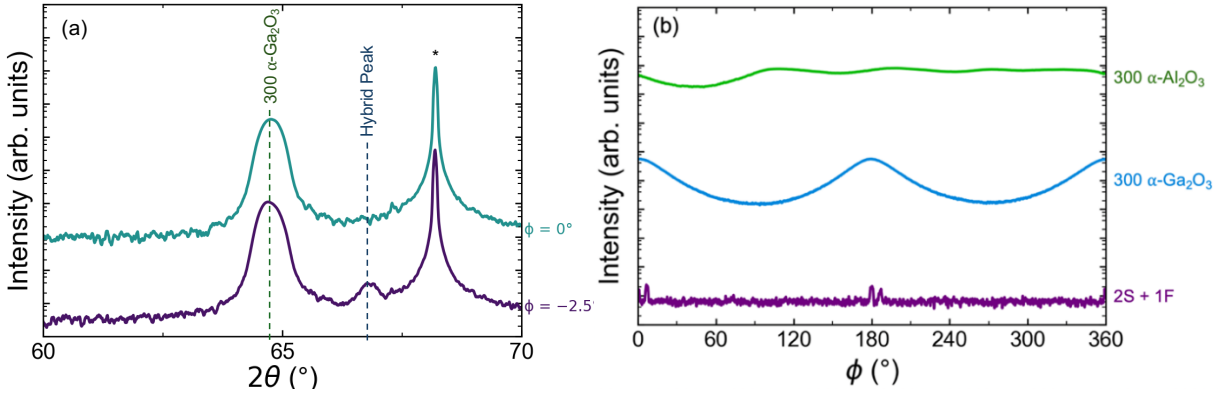

FIG. S4. (a) θ-2θ XRD measurements from 2θ = 60 – 70° at two different ϕ values of sample G3. The peak at 64.7°, marked by the dashed green line, is that of 300 α-Ga_2O_3; the peak at 68.2°, marked by a *, is that of 300 α-Al_2O_3; and the dashed blue line is the calculated position, 2θ = 67.04°, for the 200 substrate + 100 film (2S + 1F) hybrid reflection. The 2S+1F hybrid reflection only appears in the ϕ = –2.5° scan at 2θ = 66.9°, within 0.15° of the calculated position. **(b)** Full 360° ϕ XRD measurements of the 300 α-Ga_2O_3, 300 α-Al_2O_3, and 2S + 1F hybrid reflection peaks.

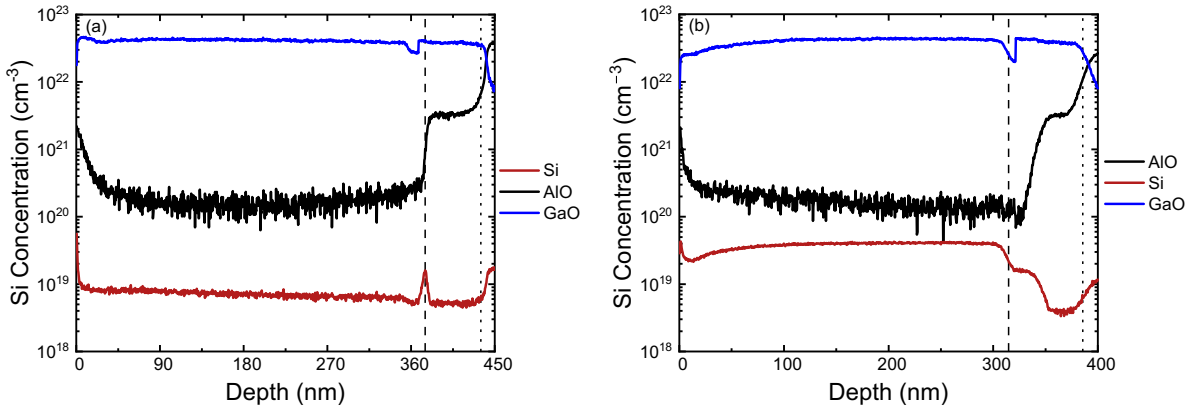

Fig. S5 (a). A plot of the concentrations of Si, AlO, and GaO that were measured with SIMS in sample G23. **(b).** A plot of the Si, AlO, and GaO concentrations that were measured with SIMS in sample G8. For both plots, a depth of 0 corresponds to the surface of the film. In both plots, the dashed line represents the interface between the Si-doped α-Ga_2O_3 and the UID α-$(Al_xGa_{1-x})_2O_3$ buffer layer and the dotted line marks the interface of the UID α-$(Al_xGa_{1-x})_2O_3$ buffer layer and the α-Al_2O_3 substrate.

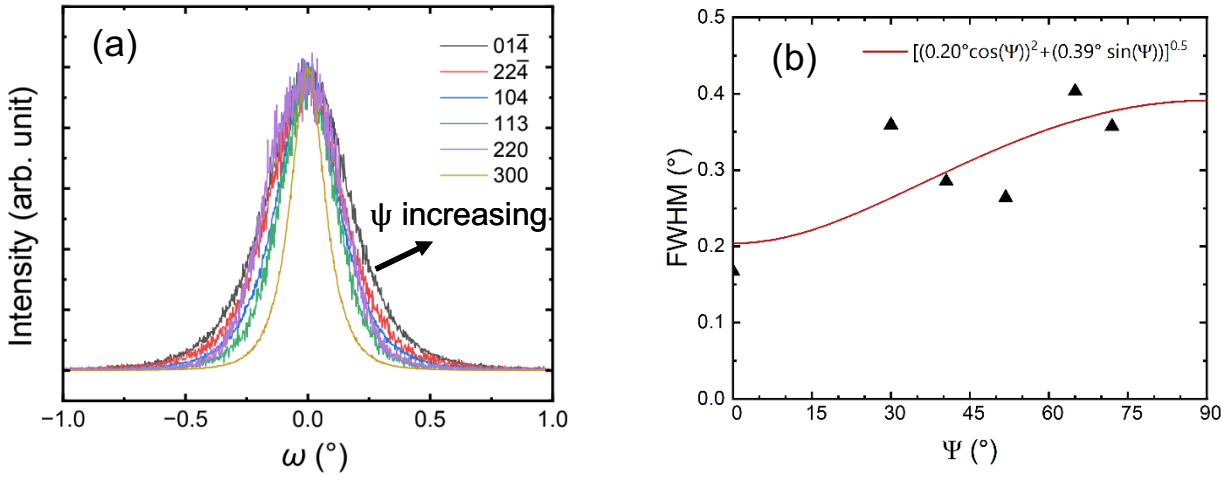

FIG. S6. (a) Rocking curves of the 300, 220, 113, 104, 22$\bar{4}$, and 01$\bar{4}$ α-Ga_2O_3 reflections in sample G5 with ψ ranging from 0° - 72° from the (100) plane of the α-Al_2O_3 substrate. **(b)** A comparison of the measured FWHM of rocking curves as a function of their respective ψ. The data is fit to the equation $K_{skew}^2=(K_{tilt}\cos(\psi))^2+(K_{twist}\sin(\psi))^2$, where K_{skew} is equal to the measured FWHM in degrees. The red line shows the best fit to the data and gives K_{tilt} = 0.20° and K_{twist} = 0.39°.

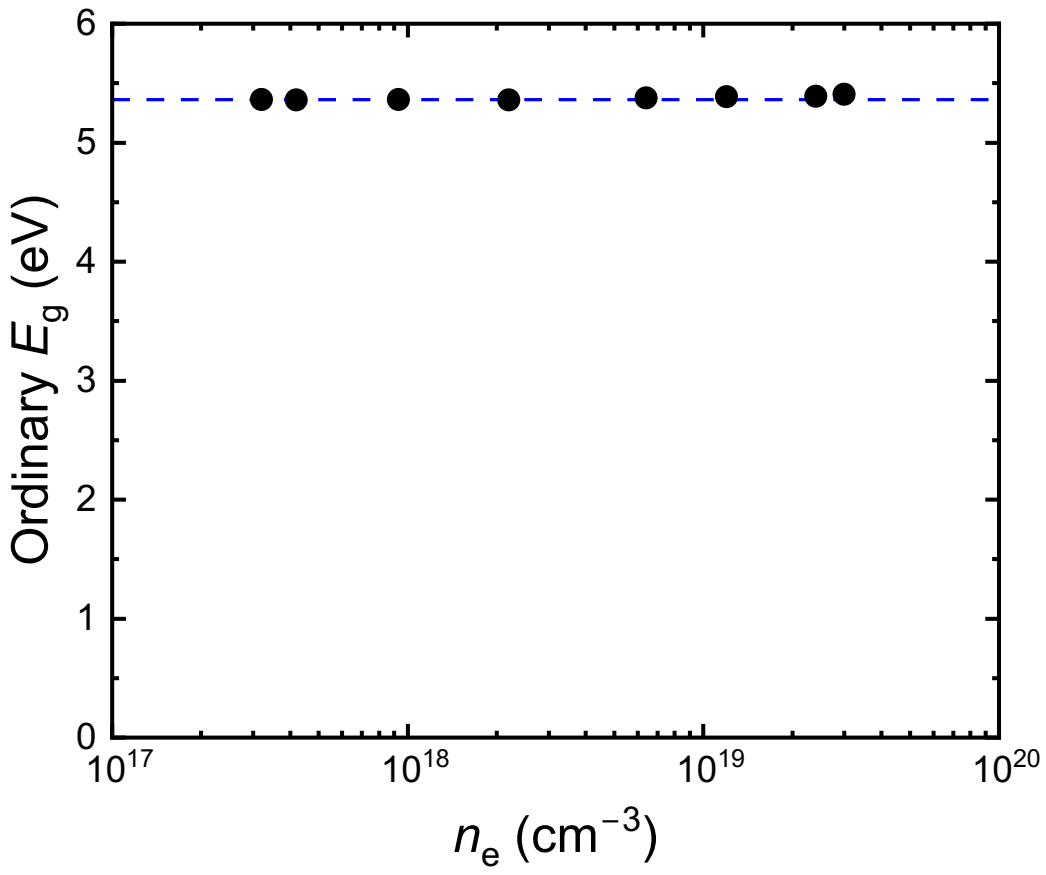

FIG. S7. A plot of the ordinary E_g of films G22-G29 as a function of their mobile electron carrier concentration, n, measured by the Hall effect. Sample G30 also has its E_g plotted as a function of its targeted N_D. The black squares are the values of E_g determined by a Tauc fit of ellipsometry measurements. The dashed blue line marks the minimum measured E_g, 5.36 eV.